Neurobiology of Disease 156 (2021) 105419

Contents lists available at ScienceDirect

Neurobiology of Disease

journal homepage: www.elsevier.com/locate/ynbdi

Specific activation of GluN1-N2B NMDA receptors underlies facilitation of cortical spreading depression in a genetic mouse model of migraine with reduced astrocytic glutamate clearance

Giovanna Crivellaro [a,1,2], Angelita Tottene [a,2], Marina Vitale [a], Marcello Melone [b], Giorgio Casari [c], Fiorenzo Conti [b,d], Mirko Santello [e], Daniela Pietrobon [a,f,*]

[a] Department of Biomedical Sciences, University of Padova, 35131 Padova, Italy
[b] Department of Experimental and Clinical Medicine, Università Politecnica delle Marche, Italy Center for Neurobiology of Aging, INRCA IRCCS, Ancona, Italy
[c] Vita Salute San Raffaele University and San Raffaele Scientific Institute, Milano, Italy
[d] Fondazione di Medicina Molecolare, Università Politecnica delle Marche, Ancona, Italy
[e] Institute of Pharmacology and Toxicology and Neuroscience Center Zurich, University of Zurich, CH-8057 Zurich, Switzerland.
[f] Padova Neuroscience Center, University of Padova, CNR Institute of Neuroscience, 35131 Padova, Italy

ARTICLE INFO

Keywords:
Migraine
Spreading depolarization
Spreading depression
α2 Na^+
K^+ ATPase
Astrocyte
Glutamate clearance
NMDA receptor
Glutamate spillover
iGluSnFr
Excitatory synaptic transmission

ABSTRACT

Migraine is a common but poorly understood sensory circuit disorder. Mouse models of familial hemiplegic migraine (FHM, a rare monogenic form of migraine with aura) show increased susceptibility to cortical spreading depression (CSD, the phenomenon that underlies migraine aura and can activate migraine headache mechanisms), allowing an opportunity to investigate the mechanisms of CSD and migraine onset. In FHM type 2 (FHM2) knock-in mice with reduced expression of astrocytic Na^+, K^+-ATPases, the reduced rate of glutamate uptake into astrocytes can account for the facilitation of CSD initiation. Here, we investigated the underlying mechanisms and show that the reduced rate of glutamate clearance in FHM2 mice results in increased amplitude and slowing of rise time and decay of the NMDA receptor (NMDAR) excitatory postsynaptic current (EPSC) elicited in layer 2/3 pyramidal cells by stimulation of neuronal afferents in somatosensory cortex slices. The relative increase in NMDAR activation in FHM2 mice is activity-dependent, being larger after high-frequency compared to low-frequency afferent activity. Inhibition of GluN1-N2B NMDARs, which hardly affected the NMDAR EPSC in wild-type mice, rescued the increased and prolonged activation of NMDARs as well as the facilitation of CSD induction and propagation in FHM2 mice. Our data suggest that the enhanced susceptibility to CSD in FHM2 is mainly due to specific activation of extrasynaptic GluN1-N2B NMDARs and point to these receptors as possible therapeutic targets for prevention of CSD and migraine.

1. Introduction

Migraine is a remarkably common, disabling, and costly brain disorder, primarily affecting the sensory nervous system. It is characterized by a global dysfunction in multisensory information processing and by attacks of typically throbbing, unilateral headache with certain associated features (Pietrobon and Moskowitz, 2013; Goadsby et al., 2017; Brennan and Pietrobon, 2018). In a third of patients, the headache is preceded by transient sensory disturbances (migraine aura), whose neurophysiological correlate is cortical spreading depression (CSD), a self-sustaining wave of nearly complete depolarization of brain cells (Pietrobon and Moskowitz, 2014). In animal models CSD may activate and sensitize the trigeminovascular pain pathway and thus initiate the headache mechanisms (Pietrobon and Moskowitz, 2014; Burstein et al., 2015; Filiz et al., 2019; Harriott et al., 2021). The neurobiological mechanisms of the primary brain dysfunctions underlying the onset of a migraine attack and susceptibility to CSD in the human brain remain largely unknown.

Familial hemiplegic migraine (FHM) is a rare monogenic form of migraine with aura caused by mutations in genes encoding either

* Corresponding author at: Department of Biomedical Sciences, University of Padova, 35131 Padova, Italy.
E-mail address: daniela.pietrobon@unipd.it (D. Pietrobon).
[1] These authors contributed equally.
[2] Present address: Coordinamento Rete Oncologica Veneta, Istituto Oncologico Veneto IRCCS, 35100 Padova, Italy.

https://doi.org/10.1016/j.nbd.2021.105419
Received 23 February 2021; Received in revised form 29 May 2021; Accepted 4 June 2021
Available online 7 June 2021

neuronal voltage-gated ion channels ($Ca_V2.1$ in FHM1; $Na_V1.1$ in FHM3) or a predominantly astrocytic ion pump (the α_2 Na+, K+ ATPase, α_2NKA, in FHM2) (Ophoff et al., 1996; De Fusco et al., 2003; Dichgans et al., 2005; Pietrobon, 2007). The functional consequences of the FHM-causing mutations can be studied in knock-in mouse models of the disease, which then provide a unique experimental system to study the cellular and circuit mechanisms of the primary brain dysfunctions causing a migraine disorder (Pietrobon and Brennan, 2019). Despite mechanistically diverse mutations, thus far all FHM knock-in models show an increased susceptibility to experimentally induced CSD (van den Maagdenberg et al., 2004; Eikermann-Haerter et al., 2009; van den Maagdenberg et al., 2010; Leo et al., 2011; Kros et al., 2018; Jansen et al., 2020) thus allowing an opportunity to investigate the underlying mechanisms.

Insights into the mechanisms underlying enhanced susceptibility to CSD were obtained in FHM1 and FHM2 models. Knock-in mice carrying gain-of-function FHM1 mutations in the $Ca_V2.1$ channel (FHM1 mice) show increased glutamate release and neurotransmission at cortical excitatory synapses (but unaltered release and transmission at inhibitory synapses) and a causative link between enhanced glutamate release and facilitation of CSD induction and propagation (Tottene et al., 2009; Vecchia et al., 2015). FHM2 knock-in mice expressing half of the α_2NKA protein that is expressed in wild-type (WT) animals (FHM2 mice) (Leo et al., 2011) show reduced density of glutamate transporters GLT-1 in astrocyte processes surrounding cortical excitatory synapses and reduced rate of glutamate and K^+ clearance in the somatosensory cortex during neuronal activity (Capuani et al., 2016; Parker et al., 2021). The reduced rate of glutamate clearance can account for most of the facilitation of CSD induction (Capuani et al., 2016). Recently, glutamate imaging in awake mice revealed spontaneous glutamatergic plumes (focal, large glutamate transients) in layer 1 (L1) of somatosensory cortex in FHM2 mice under basal conditions (not present in WT mice); a rise in plume frequency and extracellular glutamate preceded the onset of CSD, which was prevented by inhibition of the plumes and glutamate rise (Parker et al., 2021). Thus, an imbalance between release and clearance of glutamate at cortical excitatory synapses appears critical for CSD ignition.

Here, to gain further insights into the molecular and cellular mechanisms underlying enhanced susceptibility to CSD in FHM2 mice, we investigated whether the reduced rate of glutamate clearance results in enhanced activation of glutamate NMDA receptors (NMDARs) in L2/3 pyramidal cells in the somatosensory barrel cortex. The rationale is provided by the pharmacological evidence that NMDARs play a key role in initiation and propagation of experimental CSD in WT animals (Pietrobon and Moskowitz, 2014; Chung et al., 2018) and the evidence that pharmacological block of glial and neuronal glutamate transporters primarily affects NMDARs, given their higher affinity for glutamate and slower desensitization compared to AMPARs (Tsukada et al., 2005; Tzingounis and Wadiche, 2007; Trabelsi et al., 2017). Inhibition of a large fraction of glutamate transporters with a relatively high concentration of TBOA, which more than halves the rate of glutamate clearance, slowed down the decay of the NMDAR excitatory postsynaptic current (EPSC) evoked in CA1 hippocampal cells (Arnth-Jensen et al., 2002; Diamond, 2005; Tsukada et al., 2005) and L5 cortical pyramidal cells (Hanson et al., 2015; Trabelsi et al., 2017) without much effect on its amplitude, while it also increased the amplitude of the NMDAR EPSC evoked in dentate gyrus hippocampal neurons (Harney et al., 2008). The slowing of the decay of the NMDAR EPSCs was interpreted as indicative of delayed activation of synaptic and extrasynaptic NMDARs at distant sites due to increased spillover and increased dwell time of glutamate in the extracellular space (Arnth-Jensen et al., 2002). The relative slowing of glutamate clearance in L1 of barrel cortex in FHM2 mice (21%) is much smaller than that after block of a large fraction of glutamate transporters in the studies just mentioned (> 100%). So, it is unclear whether the relatively small impairment of glutamate clearance in FHM2 mice may produce delayed activation of NMDARs at distant sites and whether, in general, it may increase NMDAR activation in the barrel cortex.

We show increased amplitude and slowing of both rise time and decay of the NMDAR EPSC elicited in L2/3 pyramidal cells of barrel cortex in FHM2 mice. Furthermore, we show that inhibition of diheteromeric GluN1-N2B NMDARs, which hardly affects the NMDAR EPSC in WT mice, rescues the increased and prolonged activation of NMDARs as well as the facilitation of CSD induction and propagation in FHM2 mice.

2. Materials and methods

2.1. Animals

Experiments were performed using heterozygous knock-in mice harboring the W887R FHM2 mutation ($Atp1a2^{+/R887}$ mice: (Leo et al., 2011)) and their WT littermates (background C57BL6J, male and female in equal or near equal number). Animals were housed in specific pathogen free conditions, maintained on a 12-h light/dark cycle, with free access to food and water. All experimental procedures involving animals and their care were carried out in accordance with Italian laws and policies (D.L. n. 26, March 14, 2014) and with the guidelines established by the European Community Council Directive (2010/63/UE) and were approved by the local authority veterinary services in Padova (Italy Aut. Min. 652/2015-PR) and by the Tierversuchskommission of the canton of Zurich in Zurich (Switzerland).

2.2. Acute brain slices preparation

Acute coronal slices containing the somatosensory barrel cortex were prepared from P22–25 WT and heterozygous W887R/+ knock-in male and female mice (FHM2 mice) from the same litter, as described in (Tottene et al., 2009). Briefly, animals were anestethized with isoflurane and decapitated. The brain was quickly removed and put in an ice-cold cutting solution (in mM: 130 K gluconate, 15 KCl, 0.2 EGTA, 20 HEPES, 25 glucose, 2 kynurenic acid, 5×10^{-5} minocycline, pH 7.4 with NaOH, oxygenated with 100% O2) (Dugue et al., 2005). 350 μm-thick slices were then cut on the coronal plane with a vibratome (VT1200S, Leica Biosystems, Germany) and were transferred for 1 min in a solution containing (in mM) 225 D-mannitol, 2.5 KCl, 1.25 NaH_2PO_4, 26 $NaHCO_3$, 25 glucose, 0.8 CaCl2, 8 $MgCl_2$, 2 kynurenic acid, 5×10^{-5} minocycline, saturated with 95% O_2 and 5% CO_2. Slices were then maintained at 30 °C for 30 min in standard artificial cerebrospinal fluid saturated with 95% O2 and 5% CO_2 (sACSF in mM: 125 NaCl, 2.5 KCl, 25 $NaHCO_3$, 1.25 NaH_2PO_4, 1 $MgCl_2$, 2 $CaCl_2$, 25 glucose) plus 50 nM minocycline, and then transferred at room temperature in the same solution for a minimum of 30 min before being used for the experiment. All experiments were performed within 6 h from the mouse decapitation.

Acute cortical slices prepared as described above were used for measurement of either the NMDA receptor postsynaptic current elicited in layer 2/3 pyramidal cells by extracellular stimulation or of threshold and velocity of cortical spreading depression induced by high KCl pulses.

Slices used for two-photon glutamate imaging were prepared from 6.5 to 7 week-old male and female mice using different cutting and recovery solutions and a different vibratome (HM 650, Microm). Cutting solution (in mM): 65 NaCl, 2.5 KCl, 1.25 NaH_2PO_4, 25 $NaHCO_3$, 7 $MgCl_2$, 0.5 $CaCl_2$, 25 glucose, and 105 sucrose saturated with 95% O_2 and 5% CO_2. Slices were then transferred to a recovery solution containing (in mM) 130 K-gluconate, 15 KCl, 0.2 EGTA, 20 HEPES, 25 glucose for 2 min before being kept in oxygenated artificial cerebrospinal fluid at 34 °C for 25 min and then at room temperature until use. Slices were loaded with sulforhodamine 101 dye (SR-101, 1 μM) for 15 min at 34 °C before being kept in ACSF at room temperature.

2.3. Patch-clamp recordings

Acute coronal slices containing the barrel cortex were prepared from P22–23 mice of either sex as described in (Capuani et al., 2016) and briefly summarized above. Whole-cell patch-clamp recordings were made following standard techniques. Electrical signals were recorded through a Multiclamp 700B amplifier and digitized using an Axon Digidata 1550 interface and pClamp software (Molecular Devices). Pipette resistance: 3–5 MΩ. Currents were sampled at 10 kHz and filtered at 2 kHz. Liquid junction potentials (LJP) measured at the pipette tip was −10 mV; this value should be added to all voltages to obtain the correct membrane potentials (Neher, 1992).

Brain slices were continuously perfused in a submersion chamber with fresh extracellular solution at 30 °C at a flow rate of 3 ml/min, and were used for recording only if more than 50% of the cells were alive at 45 μm depth in a 228 × 172 μm field. Recordings were made from upper layer 2/3 pyramidal cells deeper than 45 μm from the slice surface, visualized using an upright microscope equipped with infrared light and infrared differential interference contrast (DIC) optics (water-immersion objective 60×) and identified by their typical morphological pyramidal shape and the presence of a prominent apical dendrite. In a subset of experiments, the identification was confirmed by postfixation inspection of the biocytin-labeled neurons.

Internal solution contained (in mM): 129 mM Cs-methanesulfonate, 6 mM KCl, 4 mM MgATP, 0.3 mM NaGTP, 10 mM Na-Phosphocretine, 10 mM HEPES, 0.2 mM EGTA, 3 mM QX-314, 0.2% p/v Biocytine, (pH = 7.25 with CsOH, osmolarity 320 mOsm with sucrose).

The extracellular solution for recordings of the NMDAR excitatory postsynaptic current (EPSC) was identical to that used for recordings of astrocyte synaptically-activated glutamate transporter current (STC) in (Capuani et al., 2016), except for the exclusion of NMDAR antagonists and contained: 125 mM NaCl, 2.5 mM KCl, 1 mM $MgCl_2$, 1 mM $CaCl_2$, 25 mM $NaHCO_3$, 1.25 mM NaH_2PO_4, 25 mM glucose, 10 μM NBQX, 10 μM gabazine saturated with 95% O_2 and 5% CO_2. In a fraction of the experiments (including all the pharmacological experiments) 10–30 μM D-serine was also present.

NMDAR EPSCs were evoked in voltage-clamped L2/3 pyramidal cells of the barrel cortex by electrical stimulation in lower L1 as done for elicitation of the STC in (Capuani et al., 2016), using current pulses (50 μA, 100 μs) of relatively low intensity (1.53 ± 0.03 times threshold, n = 27) through a concentric bipolar tungsten electrode (TM33CCINS, World precision Instruments, Inc., Sarasota, FL, USA) placed 200 μm away from the projection in L1 of the soma of the recorded pyramidal cell (Fig. 2A inset). The single current pulses were delivered every 5 s (low frequency stimulation; but every 30 s during drug application in the pharmacological experiments), while the train of pulses (high-frequency stimulation) were delivered every 60 s. NMDAR EPSCs were isolated by including non-NMDARs and $GABA_A$Rs blockers in the external solution and holding the membrane potential at +40 mV to remove the voltage-dependent Mg^{2+} block from NMDARs.

Series resistance was monitored continuously throughout the experiment; experiments where it changed more than 20% or had series resistance >15 MΩ (before compensation) were excluded from the data. The NMDAR EPSCs were recorded after series resistance compensation; the average values of the series resistance after compensation were similar in WT and FHM2 cells: WT: 6.4 ± 0.4 MΩ, n = 22; FHM2: 5.8 ± 0.2 MΩ, n = 25; p = 0.19, *t*-test) and < 10 MΩ in all cells. Also in all the pharmacological experiments investigating the effect of Ro25–6981 on the NMDAR EPSC the series resistance was lower than 10 MΩ after compensation and only experiments where it changed <15% during the time course of drug application were considered (average values before Ro and after 20–25 min of 1 uM Ro application: 6.7 ± 0.7 MΩ and 6.7 ± 0.5 MΩ, respectively, n = 5 in WT; 6.8 ± 0.6 MΩ and 7.6 ± 0.6 MΩ, n = 6 in FHM2; in experiments with 20 μM Ro: 8.1 ± 0.5 MΩ and 7.7 ± 0.4 MΩ n = 7 in WT; 7.0 ± 0.4 MΩ and 7.2 ± 0.4 MΩ n = 7 in FHM2; in experiments with vehicle, the series resistance was 6.7 ± 0.5 MΩ, n = 6 and 6.8 ± 0.5 MΩ after 20–25 min of vehicle application). With control experiments using subsaturating concentrations of an NMDAR antagonist (CPP, 1 uM) we ascertained that the kinetics of the NMDAR EPSC were independent of the NMDAR EPSC amplitude in the range of amplitudes measured in our experiments, thus excluding that the changes in kinetics were due to voltage-clamp errors (Arnth-Jensen et al., 2002). Measurements of current-voltage relationships for the NMDAR EPSC revealed reversal potential values averaging 10 ± 1 mV (n = 6 cells with average Rs = 4.9 ± 0.2 MΩ after compensation), suggesting relatively small voltage-space clamp errors in our recordings. To reduce variability in the number of fibers recruited by the extracellular stimulation across experiments, we payed a lot of attention to be consistent with the position of the stimulating electrode in layer 1 relative to layer 2/3 and to the recorded pyramidal cell. Despite this, the similar relatively large variability in NMDAR EPSC amplitude in different measurements in WT and FHM2 slices (Fig. 2A) suggests a certain variability in the number of fibers recruited across experiments in both genotypes. If this is the case, the lack of correlation between the amplitude of the NMDAR EPSC and the half time of decay of the NMDAR EPSC in Supplementary Fig. 1 indicates that the decay kinetics of the NMDAR EPSC do not depend on the number of recruited fibers at our stimulation intensity.

2.4. Analysis of patch-clamp recordings

The NMDAR EPSC amplitude was measured at the peak of the evoked current. The total charge of the NMDAR EPSC was measured by integrating the NMDAR current from the time of peak amplitude to the time where the current has decayed to 10% of the peak amplitude. The analysis of the decay kinetics of the NMDAR-EPSC was performed by measuring the half time of decay ($t_{1/2}$, the time at which the amplitude of the NMDAR EPSC is reduced to half, calculated from the time of peak amplitude) or by fitting with a double exponential function the current decay ($y = A_f * \exp(-(x - x0)/\tau_f) + A_s * \exp(-(x - x0)/\tau_s)$, where A_f and A_s are the relative amplitudes and τ_f and τ_s are the time constants of the fast and the slow exponential components, respectively. The weighted time constant was calculated as follows: $\tau_w = [(A_f * \tau_f) + (A_s * \tau_s)]/(A_f + A_s)$]. The analysis of the activation kinetics of the NMDAR EPSC was performed by measuring the time at which the NMDAR current reaches 95% of the peak amplitude.

2.5. Cortical spreading depression

Cortical spreading depression was elicited and measured in acute coronal slices of the somatosensory cortex of P22-25 WT and FHM2 mice as in (Capuani et al., 2016). Briefly, the brain slices were placed into a submersion chamber and continuously perfused with fresh extracellular solution (as that used for NMDAR EPSC recordings but with 1.2 mM $CaCl_2$, 3.5 mM KCl and without NBQX and gabazine) at 30 °C at a flow rate of 6 ml/min, and brief pressure-ejection pulses of 3 M KCl (0.5 bar) of increasing duration (at 5 min intervals in 20 ms steps) were applied through a glass micropipette (resistance ranging from 0.19 to 0.24 MΩ) onto the slice surface on layer 2/3, using a PDES-02DX pneumatic drug ejection system (Npi Electronic GmbH, Tamm, Germany), until a CSD was elicited. CSD was detected by monitoring the associated change in intrinsic optical signal (IOS). The duration of the first pulse eliciting a CSD was taken as CSD threshold and the rate of horizontal spread of the change in IOS as CSD velocity. IOS was recorded using a CMOS camera (Basler ace acA1920-155um USB 3.0, Basler, Germany) connected with an upright microscope (Nikon Eclipse; 10× magnification, Nikon, Tokio, Japan). Images were recorded at 200 ms intervals as 1920 × 1200 pixels images (pixel size: 1.27 μm). MBF ImageJ software was used for the off line analysis of the digitalized images.The IOS change is expressed as percent change in light trasmittance (ΔT) relative to the background signal: %ΔT/T. To test the effect of Ro25-6981 (1 μM) on CSD threshold and velocity, high KCl pulses were applied after perfusion of slices for 25 min with extracellular solution with or without Ro25-6981.

2.6. Glutamate imaging

Glutamate imaging was performed as described in (Romanos et al., 2019). Six weeks old FHM2 mice and WT littermates were injected with 0.3–0.5 μl of AAV2/1.GFAP.iGluSnFr.WPRE.SV40 (Penn Vector; provided by Dr Loren Looger, Janelia Farm) into the barrel cortex through a glass pipette. Stereotaxic co-ordinates with respect to Bregma were (in mm): 1 posterior, 3.5 lateral, 0.3 ventral. Fifteen to eighteen days following the viral injections, coronal brain slices (350 μm) containing the barrel cortex were obtained as described previously (Santello and Nevian, 2015) and briefly summarized above. A galvanometer-based two-photon laser scanning system was used to image extrasynaptic glutamate (16× objective, zoom 6, excitation wavelength 900 nm, 64 × 64 pixels/image, acquisition rate 19.2 Hz). Astrocytes were visualized using the sulforhodamine 101 dye (SR101, 1 μM, incubation 15 min at 34 °C).

Synaptic glutamate release was elicited by single pulse stimulation and by trains of 10 pulses at high frequency (100 Hz) every 20 s delivered via a theta-glass pipette (bipolar, 100 μs, stimulation intensity 3–5 V) placed in the inner L1. In order to visualize the theta-glass pipette, the latter was filled with ACSF containing 5 μM SR-101. All solutions contained 10 μM NBQX, 50 μM APV, 100 μM picrotoxin and temperature was kept between 33 and 34 °C while imaging. 10 consecutive sweeps were acquired and subsequently analyzed using Image J. Fluorescence emission was collected from a region of interest (ROI, diameter 34 μm) 10–40 μm away from the stimulation pipette. The average background values (derived from a region within the field of view which was free of clearly visible iGluSnFr, typically outside the slice) were then subtracted from the fluorescence intensity of the ROIs for each frame. Traces were then averaged and the time constant (τ) of decay was calculated by fitting a single exponential function using Igor Pro (wavemetrics). τ decay was independent of the ROI location and relative distance from the stimulation pipette (Romanos et al., 2019). Genotypes were blinded to the experimenter until the analysis was completed.

2.7. Western blottings

For western blotting studies, P39 WT (N = 4; 2 males and 2 females) and FHM2 (N = 4; 2 males and 2 females) mice were anesthetized with chloral hydrate (300 mg/kg i.p.) and decapitated. The cerebral cortex was quickly separated, tissue was homogenized (Melone et al., 2001), and crude synaptic membranes were prepared (Danbolt et al., 1990). The total amount of protein in cortical crude synaptic membranes was determined according to the Bradford method (Bradford, 1976) using the Bio-Rad Protein Assay (Bio-Rad Laboratories, GmbH, Munchen, Germany) and a Bio-Rad SmartSpec 3000 UV/Vis Spectrophotometer (3 measurements/homogenate). A standard curve with 2–10 μg of bovine serum albumin was drawn for each dosing run. Curves of increasing concentration of homogenates were drawn to define a linear range for densitometric analysis of GluN2A and GluN2B and for selecting the optimal concentration for final experiments (Bragina et al., 2006). Aliquots of homogenates (7.5 μg of total protein for both GluN2A and GluN2A) were subjected to SDS-PAGE; from each animal homogenates were experimented 4 times for both antigens. To control protein loading, β-actin was used as housekeeping protein (Li and Shen, 2013; Capuani et al., 2016). Separated proteins were electroblotted onto nitrocellulose filters by Bio-Rad Trans-Blot Turbo Transfer System; then nitrocellulose were initially washed in phosphate buffered saline with 0.1% Tween 20 (PBS-T; pH 7.4); subsequently, they were exposed first to a blocking buffer solution (EveryBlot Blocking Buffer, Bio-Rad; 5 min), and incubated (2 h at room temperature and then overnight at 4 °C) in a solution of 0.1% BSA in PBS-T containing anti-GluN2A or anti-GluN2B made in rabbit (1:700; anti-GluN2A, raised against the C-terminal 1126-1408 sequence, Af542; RRID:AB_2571605; Frontier Institute co., Ltd.; (Meguro et al., 1992); (Watanabe et al., 1998); anti-GluN2B, raised against the C-terminal 1301–1456 sequence, Af300; RRID:AB_2571762; Frontier Institute co., Ltd.; (Kutsuwada et al., 1992); (Watanabe et al., 1998)) and anti-β-actin made in mouse (11,000, A5441, RRID, AB_476744; Sigma-Aldrich, St Louis, MO) primary antibodies. The following day, filters were washed with PBS-T and then exposed to the appropriate cocktail of secondary fluorescent antibodies (1:700; for 2 h; source Jackson, Immunoresearch, Europe Ltd.; Alexa 488 AffiniPure F (ab')$_2$ Anti-Rabbit, 711-546-152; RRID:AB_2340619; Cy3 AffiniPure F (ab')$_2$ Fragment Donkey Anti-Mouse, 715-166-150; RID:AB_2340816) dissolved in PBS-T. Immunoreactive bands were visualized by Bio-Rad Chemidoc MP Imaging System and then by Bio-Rad Image Lab software version 6.0. The optimal time of exposure during acquisition was automatically set based on the appearance of a few saturated pixels in immunoreactive bands for each fluorescent channel (green for GluN2A and GluN2B and red for β-actin) with a visible background. Acquired original images were used to quantify the intensity of bands by Bio-Rad Image Lab. Collected values were used to calculate ratios of GluN2A/β-actin and GluN2B/β-actin (Capuani et al., 2016). Comparison between WT and FHM2 measures for each antigen was performed using GraphPrism v. 8.2 (GraphPad Software, Inc). For final qualitative illustrations of data, original images were properly cropped, dimensioned, and converted into high-resolution images (600 dpi) using Adobe Photoshop CS5 extended (v.22.0). Color levels of final images were obtained by using the level function with a minimal degree of processing.

2.8. Statistics

After assessing for normal distribution (using the Shapiro–Wilk test), comparison between two groups was made using two-tailed unpaired or paired *t*-test for normal distributed data or the Mann–Whitney *U* test (MW) for nonparametric data. Equal variances were assumed. Data are given as mean ± SEM; differences were considered statistically significant if $P < 0.05$ (*$P < 0.05$; **$P < 0.01$; ***$P < 0.001$). No statistical methods were used to choose sample sizes that were estimated based on previous experience and are in line with those in the literature. No animals were excluded from the analysis.

2.9. Chemicals and drugs

Reagents for extracellular and internal solution were obtained from Sigma-Aldrich, except for NBQX, Gabazine, QX-314, D-serine and Ro25–6981 which were obtained from Tocris. SR-101 was obtained from Invitrogen.

3. Results

3.1. Prolonged dwelling time of glutamate in the extracellular space following synaptic stimulation in the barrel cortex in FHM2 mice

To investigate how the reduced rate of glutamate uptake by L1 astrocytes in FHM2 (Capuani et al., 2016) affects the time course of extracellular glutamate following synaptic stimulation in the somatosensory cortex, we used the genetically-encoded glutamate sensor iGluSnfr expressed in astrocytes in combination with two photon microscopy (Marvin et al., 2013) in cortical slices from WT and FHM2 mice. Synaptic activity was elicited by focal electrical stimulation with a theta electrode in L1 and glutamate was imaged in a region of interest in the proximity of the stimulating electrode as in (Romanos et al., 2019). The decay kinetics of the glutamate transients elicited by low frequency (single pulse) stimulation or high-frequency (train of 10 pulses at 100 Hz) stimulation were both slower in FHM2 compared to WT mice (Fig. 1). The average time constant obtained from monoexponential fits of the decay of the iGluSnFr signals elicited by low frequency stimulation was 23% larger in FHM2 mice (Fig. 1A, cf. legend for average values and statistics). The average decay time constant of the glutamate transients elicited by high frequency stimulation was 28% larger in FHM2 compared to WT mice (Fig. 1B).

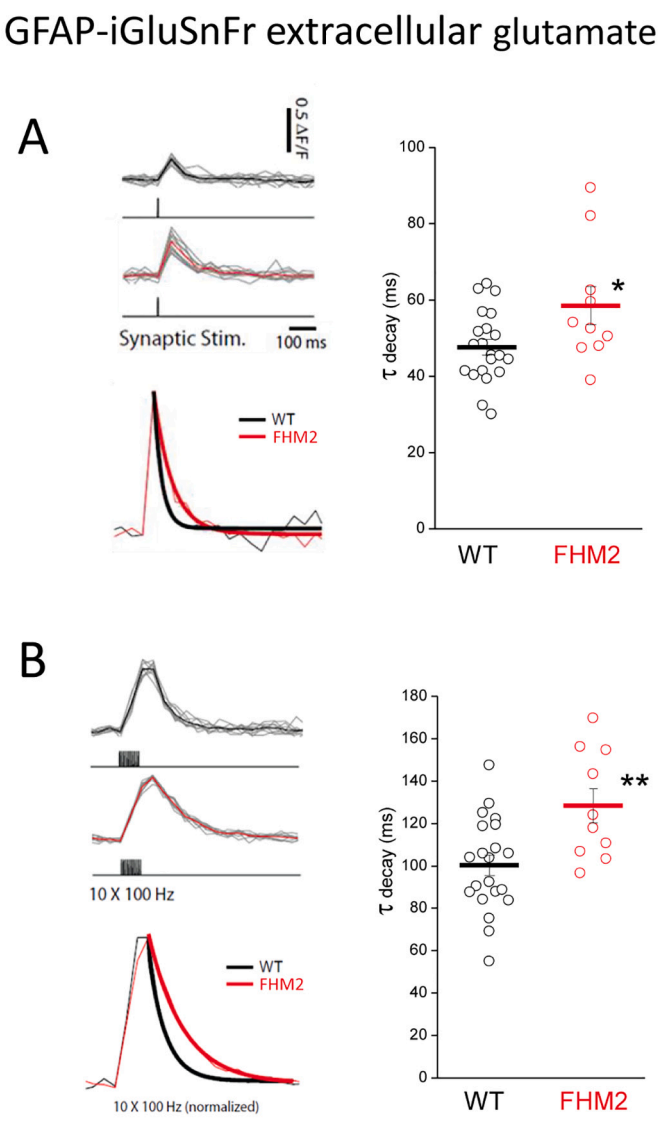

Fig. 1. Glutamate clearance following synaptic stimulation is slower in FHM2 compared to WT mice.

Extracellular glutamate was imaged using the glutamate sensor iGluSnFr expressed in the plasma membrane of astrocytes (GFAP-iGluSnFR) in acute brain slices containing the somatosensory cortex. Synaptic glutamate release was elicited by stimulation with a theta glass electrode placed in inner L1 and glutamate was imaged from a region of interest 10–40 um away from the electrode.

A, B Upon synaptic stimulation (single stimulation in A; repetitive stimulation: 10 pulses at 100 Hz in B) robust and consistent increases in iGluSnFr emission could be detected in both WT (black) and FHM2 (red) mice (Left panels, in which thick lines in the top traces represent the average of the responses and in the bottom traces the mono-exponential fit of the decay of the normalized average responses). The decay kinetics of the glutamate transients are slower in FHM2 compared to WT mice. Right panels: A Average values of the time constant of decay of the iGluSnFR response elicited by low frequency single pulse stimulation: $\tau = 59 \pm 5.0$ ms, n = 10, N = 5 in FHM2; $\tau = 48 \pm 2.0$ ms, n = 21, N = 10 in WT; p = 0.02, *t*-test; B Average values of the time constant of decay of the iGluSnFR response elicited by high frequency (10 pulses at 100 Hz) stimulation: $\tau = 128 \pm 8$ ms, n = 10, N = 5 in FHM2; $\tau = 100 \pm 5$ ms, n = 21, N = 10 in WT; p = 0.004, *t*-test. Hereafter, n indicates the number of slices and N indicates the number of mice. Data are mean ± SEM.

These findings confirm with a different technique the activity-dependent slowdown of glutamate clearance in FHM2, previously uncovered with measurements of the synaptically activated glutamate transporter current (STC) in L1 astrocytes (Capuani et al., 2016), and directly show that the defective glutamate buffering capacity by astrocytes in FHM2 results in prolonged dwelling time of glutamate in the extracellular space. Our glutamate imaging in L1 also confirms previous evidence (from both STC and iGluSnFr measurements) that in the somatosensory cortex glutamate clearance is slower after high frequency compared to low frequency synaptic stimulation (cf τ decay = 100 ± 5 ms vs τ decay = 48 ± 2.0 ms in WT, p = 3×10^{-11} paired *t*-test) (Armbruster et al., 2016; Capuani et al., 2016; Romanos et al., 2019).

3.2. *Increased amplitude and slowing of the NMDAR excitatory postsynaptic current elicited in layer 2/3 pyramidal cells in FHM2 mice*

Given the key role of NMDARs in induction of experimental CSD (Pietrobon and Moskowitz, 2014) and their high affinity for glutamate, which make them particularly sensitive to glutamate spillover (Tzingounis and Wadiche, 2007), we next investigated the effect of the reduced rate of glutamate clearance on the activation of postsynaptic NMDARs in FHM2 mice. Synaptic NMDAR currents (NMDAR-EPSC) were evoked in L2/3 pyramidal cells of the barrel cortex by electrical stimulation in L1 as done for elicitation of the STC in (Capuani et al., 2016). NMDAR EPSCs were isolated by including non-NMDARs and $GABA_A$Rs blockers in the external solution and holding the membrane potential at +40 mV to remove the voltage-dependent Mg^{2+} block from NMDARs, as previously done in several studies investigating the effect of pharmacological block of glutamate transporters (Arnth-Jensen et al., 2002; Diamond, 2005; Tsukada et al., 2005; Hanson et al., 2015; Trabelsi et al., 2017).

The amplitude of the NMDAR EPSC elicited by single pulse stimulation was 45% larger in FHM2 compared to WT mice (Fig. 2A). Moreover, in the same cells, the decay kinetics of the NMDAR EPSC were slower in FHM2 compared to WT mice. The half-time of decay ($t_{1/2}$, the time at which the amplitude of the NMDAR EPSC is reduced to half, calculated from the time of peak amplitude), was 22% larger in FHM2 mice (Fig. 2B). Fitting the decay of the pooled average traces of the NMDAR EPSC with two exponentials revealed larger time constants for both the fast and slow components in FHM2 compared to WT mice (fast component: $\tau_f = 47$ ms vs $\tau_f = 39$ ms; slow component: $\tau_s = 228$ ms vs $\tau_s = 204$ ms); however, the relative amplitudes of the exponential components were similar in the two genotypes ($A_f = 0.77$ in FHM2 vs $A_f = 0.76$ in WT). The weighted time constant, τ_w, was 16% larger in FHM2 (89 vs 77 ms). The activation kinetics of the NMDAR current were also slower in FHM2 compared to WT mice, with the time at which the current amplitude reaches 95% of the peak value 12% larger in FHM2 mice (Fig. 2B inset). We also integrated the NMDAR current to obtain the total charge of the NMDAR EPSC, which is less affected by dendritic filtering than the amplitude. The total charge of the NMDAR EPSC evoked by single pulse stimulations was 64% larger in FHM2 compared to WT (Fig. 2A), an increase that reflects the changes in both amplitude and kinetics of the NMDAR current in FHM2 mice. These data support the conclusion that the reduced rate of glutamate clearance at excitatory synapses in FHM2 mice results in increased and prolonged activation of NMDARs in layer 2/3 pyramidal cells. The slowing of the activation and decay kinetics of the NMDAR EPSC in FHM2 mice is consistent with increased diffusion distance between the sites of glutamate release and the target NMDARs due to increased glutamate spillover and increased dwelling time of glutamate in the extracellular space.

Given the evidence that the relative slowing of glutamate clearance in FHM2 is activity-dependent being larger after high-frequency compared to low frequency stimulation ((Capuani et al., 2016) and here Fig. 1), we measured the NMDAR EPSC elicited by trains of 10 pulses at 100 Hz. The amplitude of the NMDAR EPSC elicited by this high-frequency train was 60% larger in FHM2 compared to WT mice

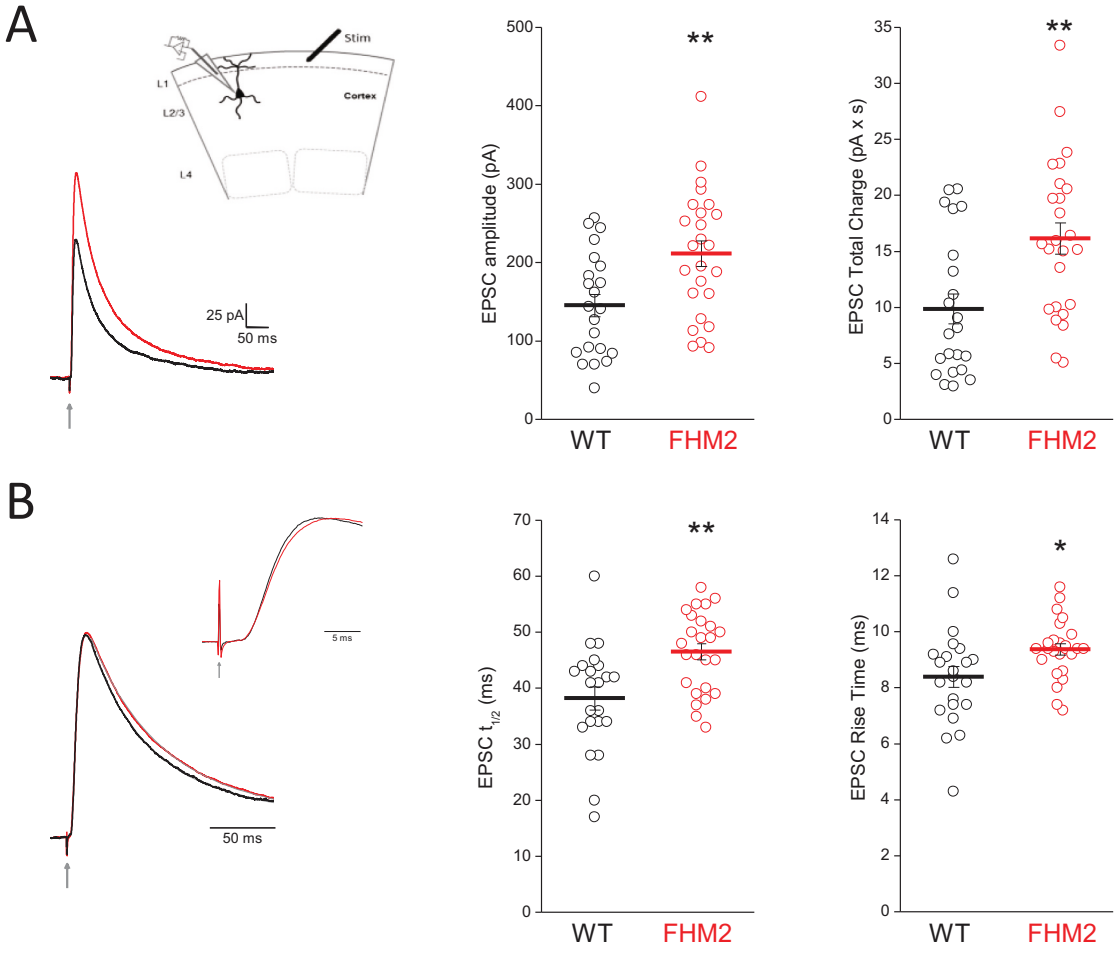

Fig. 2. The NMDAR excitatory postsynaptic current is larger and has slower activation and decay kinetics in FHM2 compared to WT mice.
NMDAR excitatory postsynaptic currents (NMDAR-EPSC) evoked by electrical stimulation in L1 (inset in A) were measured in voltage-clamped L2/3 pyramidal cells at +40 mV in acute slices of barrel cortex in the presence of glutamate non-NMDARs and $GABA_A$Rs blockers.
A The amplitude and the total charge of the NMDAR EPSC elicited by low frequency single pulse stimulation are larger in FHM2 compared to WT mice. Average values of EPSC amplitude in FHM2: 211 ± 16 pA, n = 25, N = 15; in WT: 145 ± 14 pA, n = 22, N = 13; p = 0.004, *t*-test. Average values of EPSC total charge in FHM2: 16.2 ± 1.4 pA × s; in WT: 9.9 ± 1.3 pA × s, p = 0.00006, *t*-test. The traces on the left are the average NMDAR current responses elicited by single pulse stimulation (indicated by the arrow) in WT (black, n = 22) and FHM2 (red, n = 25) mice.
B The decay and activation kinetics of the NMDAR EPSC elicited by low frequency single pulse stimulation are both slower in FHM2 compared to WT mice. Average values of the half-time of decay ($t_{1/2}$, the time at which the amplitude of the NMDAR EPSC is reduced to half, calculated from the time of peak amplitude) in FHM2: 46.6 ± 1.4 ms; in WT: 38.2 ± 2.1 ms; p = 0.001 *t*-test. Average values of the time at which the current amplitude reaches 95% of the peak value (EPSC rise time) in FHM2: 9.4 ± 0.2 ms; in WT: 8.4 ± 0.4 ms, p = 0.02, *t*-test. The traces on the left are the normalized average NMDAR current responses elicited by single pulse stimulation (indicated by the arrow) in WT (black, n = 22) and FHM2 (red, n = 25) mice. The inset shows the first 20 ms after stimulation of the same traces. The half time of decay, $t_{1/2}$, and the rise time obtained from the average traces are identical to those obtained by averaging the values of the single cells.

(Fig. 3A). In the same cells, the half-time of decay of the NMDAR EPSC was 27% larger in FHM2 compared to WT mice (Fig. 3B).

Fitting the decay of the pooled average traces of the NMDAR EPSC with two exponentials revealed larger time constants for both the fast and slow components in FHM2 compared to WT mice (fast component: τ_f = 141 ms vs τ_f = 111 ms; slow component: τ_s = 390 ms vs τ_s = 331 ms); however, the relative amplitudes of the exponential components were similar in the two genotypes (A_f = 0.85 in FHM2 vs A_f = 0.87 in WT). The weighted time constant (τ_w) was 28% larger in FHM2 (179 vs 140 ms). As a consequence of the changes in amplitude and kinetics of the NMDAR EPSC in FHM2 mice, the total charge of the NMDAR current evoked by high frequency stimulation was 106% larger in FHM2 compared to WT (Fig. 3A). Both the increase in amplitude and the slowing of the decay of the NMDAR EPSC in FHM2 mice were larger with high frequency compared to low frequency afferent activity (resulting in a 65% relatively larger gain-of-function of the total charge carried by NMDARs with high frequency compared to low frequency activity in FHM2 mice). These data support the conclusion that the relative increase in activation of NMDARs in FHM2 mice is activity-dependent, reflecting the activity dependence of the relative slowing of glutamate clearance and hence glutamate spillover in FHM2 compared to WT mice.

3.3. Preferential inhibition of GluN1-N2B NMDARs rescues the increased and prolonged activation of NMDARs in FHM2 mice without affecting the NMDAR EPSC in WT mice

The affinity for glutamate is one of the properties that may differ in NMDARs with different subunit composition, which therefore may be differently sensitive to glutamate spillover (Paoletti et al., 2013). The

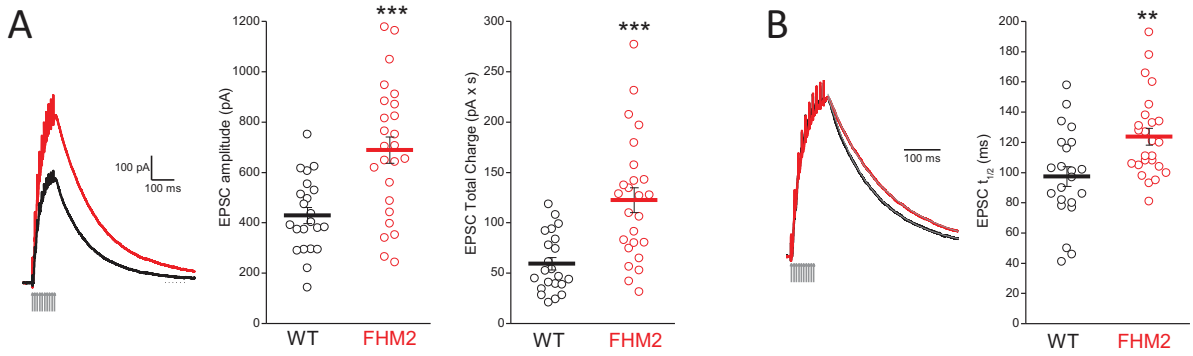

Fig. 3. The increase in amplitude and the slowing of the NMDAR EPSC in FHM2 mice are both larger with high-frequency compared with low frequency stimulation.
A The amplitude and the total charge of the NMDAR EPSC elicited by a high frequency (100 Hz) train of 10 pulses are larger in FHM2 compared to WT mice. Average values of EPSC amplitude in FHM2: 689 ± 52 pA, n = 25, N = 15; in WT: 430 ± 32 pA, n = 22, N = 13; p = 0.0002, *t*-test. Average values of EPSC total charge in FHM2: 123 ± 12 pA × s; in WT: 59 ± 6 pA × s; p = 0.00006, *t*-test. The traces on the left are the average NMDAR current responses elicited by high frequency stimulation (indicated by the arrow) in WT (black, n = 22) and FHM2 (red, n = 25) mice.
B The decay kinetics of the NMDAR EPSC elicited by high frequency stimulation are slower in FHM2 compared to WT mice. Average values of the half-time of decay ($t_{1/2}$) in FHM2: 124 ± 6 ms; in WT: 98 ± 7 ms; p = 0.003, *t*-test. The traces on the left are the normalized average NMDAR current responses elicited by high frequency stimulation (indicated by the arrow) in WT (black, n = 22) and FHM2 (red, n = 25) mice. $t_{1/2}$ obtained from the average traces is identical to that obtained by averaging the values of the single cells.

diheteromeric GluN1-N2B NMDARs have a higher affinity for glutamate than both the diheteromeric GluN1-N2A and the triheteromeric GluN1-N2A-N2B receptors (Stroebel et al., 2018), and hence are expected to be preferentially activated by glutamate spillover. To determine whether the FHM2 mutation mainly affects GluN1-N2B NMDARs, we investigated the sensitivity of the NMDAR EPSC to 1 μM Ro25–6981 (Ro25), a GluN2B-selective allosteric NMDAR antagonist; at this concentration, Ro25 inhibits only a very small fraction of the triheteromeric GluN1-N2A-N2B receptors in WT animals (Volianskis et al., 2013; Stroebel et al., 2018).

In WT slices, after 20–25 min application of 1 μM Ro25 in the perfusing solution, the NMDAR EPSC elicited by low frequency stimulation was barely decreased by 7 ± 5% (n = 5, N = 5) compared to the baseline value (control, before Ro25 perfusion) (Fig. 4A, C). In parallel experiments in which the slices were perfused with vehicle the decrease of the NMDAR EPSC after 20–25 min was 12 ± 6% (n = 6, N = 5), likely

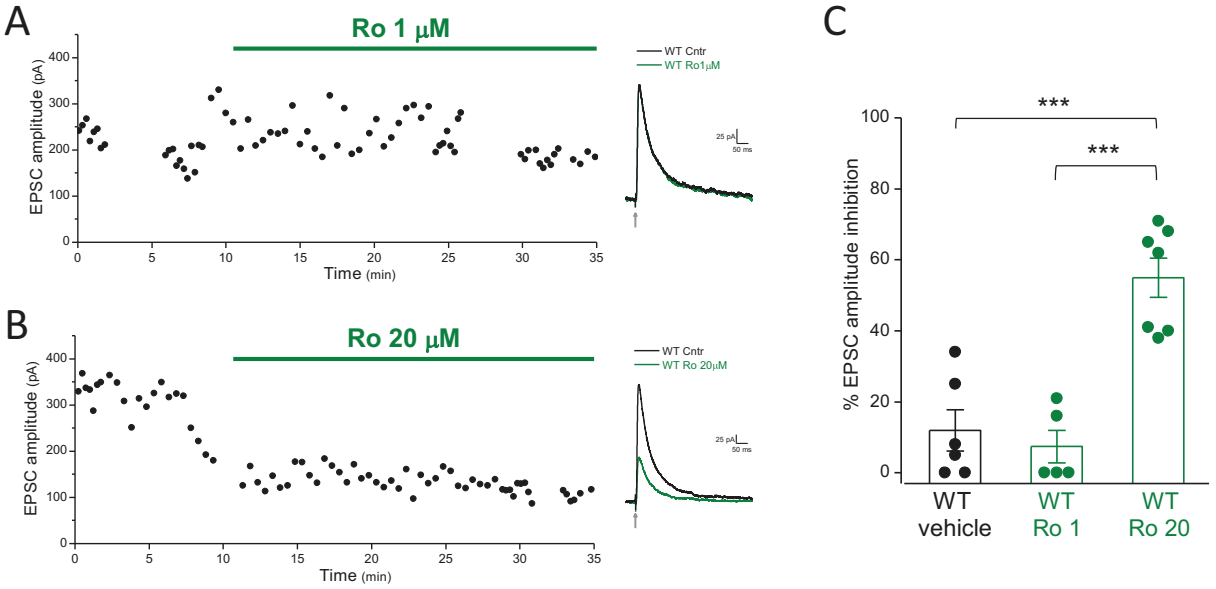

Fig. 4. The NMDAR EPSC is not affected by preferential inhibition of diheteromeric GluN1-N2B NMDARs in WT mice.
A Time course of a representative experiment in which the NMDAR EPSC elicited by low frequency stimulation was measured in WT slices before and after application of 1 μM Ro25 (Ro) for the time indicated by the green bar (left) and representative traces of the NMDAR EPSC measured before (black, control) and 20–25 min after the beginning of Ro25 application (green, Ro) (right). At this concentration, Ro25 inhibits only a very small fraction of the triheteromeric GluN1-N2A-N2B NMDARs. Current pulses were delivered every 5 s before Ro (except for the time in which high-frequency stimulation every 60 s was applied, which appears empty in the time course) and every 30 s during Ro application.
B As in A, except that a higher concentration (20 μM) of Ro25 was applied. At this concentration, Ro25 also inhibits (although incompletely) triheteromeric GluN1-N2A-N2B NMDARs.
C Percentage of inhibition of the NMDAR EPSC after application for 20–25 min of vehicle and Ro25 at two different concentrations (1 μM and 20 μM): 12 ± 6% vehicle, 7 ± 5% Ro 1 μM (p = 0.56 *t*-test; p = 0.27 paired *t*-test for vehicle relative to baseline and p = 0.33 paired *t*-test for Ro 1 uM relative to baseline); 55 ± 5% Ro 20 μM (p = 0.0001 relative to 1 μM Ro; *t*-test; p = 0.0002 relative to vehicle, *t*-test; p = 8×10^{-5} relative to baseline, paired *t*-test).

due to rundown (Fig. 4C). Thus, diheteromeric GluN1-N2B receptors do not significantly contribute to the NMDAR EPSC elicited in L2/3 Pyrs by low frequency stimulation in P22-23 WT mice. Accordingly, the kinetics of the NMDAR EPSC were similar in the presence and absence of Ro25.

Like other GluN2B-selective allosteric antagonists, Ro25 at concentrations higher than those inhibiting the diheteromeric GluN1-N2B receptors also inhibit, although incompletely, the triheteromeric GluN1-N2A-N2B NMDARs (Volianskis et al., 2013; Hansen et al., 2014; Stroebel et al., 2018), which are widespread in the CNS and are the predominant NMDARs in adult hippocampal CA3-CA1 synapses (Gray et al., 2011; Volianskis et al., 2013; Stroebel et al., 2018). Interestingly, as reported for these hippocampal synapses (Volianskis et al., 2013), 20 μM Ro25 inhibited a large fraction of the NMDAR EPSC elicited in L2/3 pyramidal cells in WT mice (55 ± 5%, n = 7, N = 5) (Fig. 4B, C), suggesting that triheteromeric GluN1-N2A-N2B NMDARs are the predominant synaptic NMDARs at the synapses onto L2/3 pyramidal cells activated by extracellular stimulation in L1. Consistent with this, the parameters of the biexponential fit of the decay kinetics of the NMDAR EPSC measured in WT L2/3 pyramidal cells ($\tau_f = 39$ ms, $\tau_s = 204$ ms, $A_f = 0.76$), are similar to those reported for recombinant and native GluN1-N2A-N2B receptors (Hansen et al., 2014) (Tovar et al., 2013).

In contrast to the insensitivity of the WT NMDAR EPSC, a significant fraction (48 ± 6%, n = 6, N = 5) of the NMDAR EPSC elicited in L2/3 Pyrs by low frequency stimulation was inhibited by 1 uM Ro25 in FHM2 mice (Fig. 5). Although the fractional inhibition of the NMDAR EPSC is most likely overestimated as a consequence of rundown (and becomes 36% if corrected for the % inhibition with vehicle), our findings suggest that activation of diheteromeric GluN1-N2B receptors may account for the increase in NMDAR EPSC amplitude in FHM2 compared to WT mice. Indeed, the values of both the EPSC amplitude and EPSC total charge in the presence of Ro25 (1 uM) in FHM2 slices were not significantly different from those in WT slices (Fig. 5B; see legend for average values

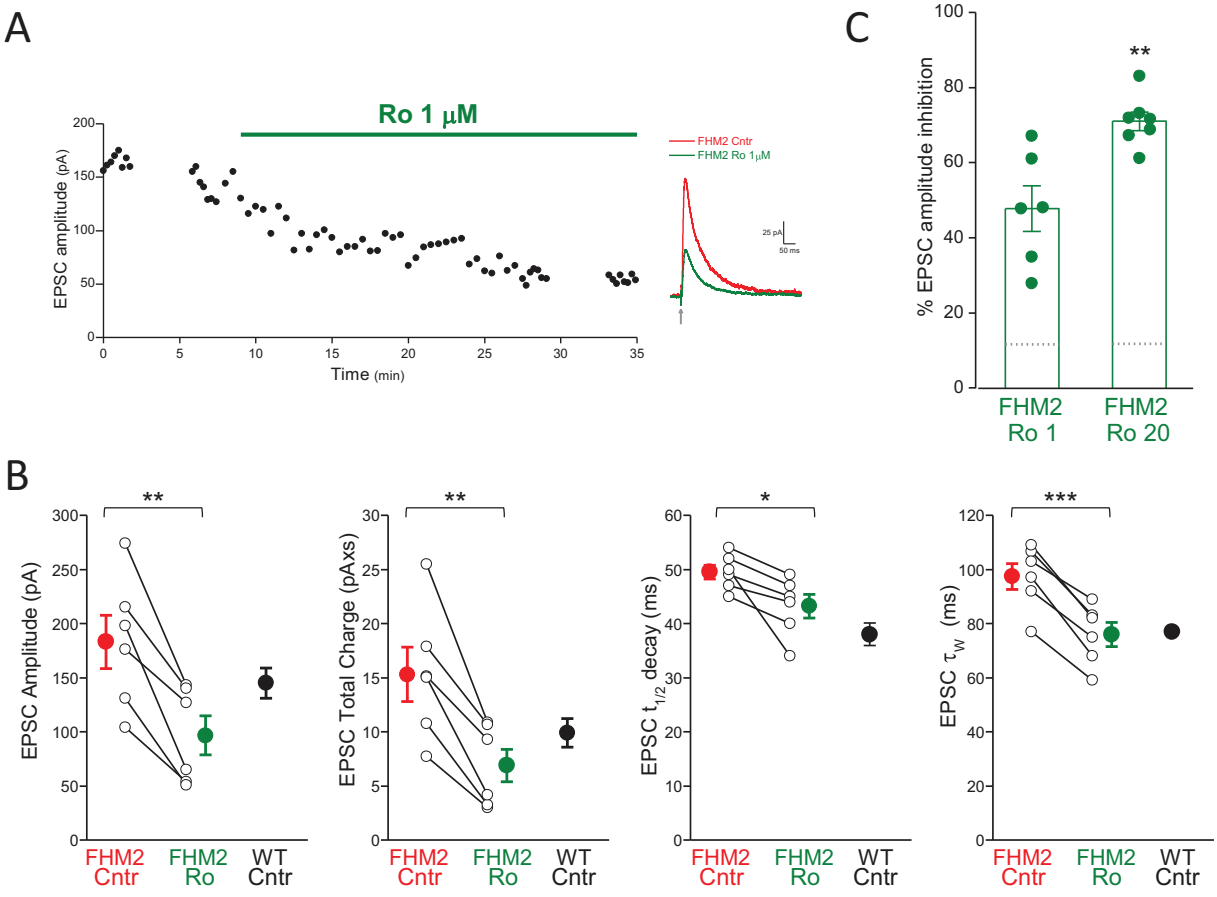

Fig. 5. Preferential inhibition of diheteromeric GluN1-N2B NMDARs rescues the increased amplitude and slower kinetics of the NMDAR EPSC in FHM2 mice.
A Time course of a representative experiment in which the NMDAR EPSC elicited by low frequency stimulation was measured in FHM2 slices before and after application of 1 μM Ro25 (Ro) for the time indicated by the green bar (left) and representative traces of the NMDAR EPSC measured before (red, control) and 20 min after the beginning of Ro application (green, Ro) (right).
B NMDAR EPSC amplitude, charge, half time of decay ($t_{1/2}$) and weighted time constant of decay (τw) before (FHM2 Cntr) and 20–25 min after the beginning of Ro (1 μM) application (FHM2 Ro). For comparison, also the corresponding values in WT mice (from Fig. 2) are shown (WT Cntr). Average values of FHM2 NMDAR EPSC amplitude, charge, $t_{1/2}$ and τw are all lower after Ro: 183 ± 25 pA in Cntr vs 97 ± 18 pA in Ro, p = 0.002 paired *t*-test; 15 ± 3 pA × s in Cntr vs 7 ± 2 pA × s in Ro, p = 0.002 paired *t*-test; 50 ± 1 ms in Cntr vs 43 ± 2 ms in Ro, p = 0.02, paired *t*-test; 97 ± 5 ms in Cntr vs 76 ± 5 ms in Ro, p = 0.0003, paired test; n = 6, *N* = 5. The average values of the time constants and amplitudes of the fast and slow exponentials best fitting the decay were: τf = 53 ± 2 ms in Cntr vs 44 ± 3 ms in Ro, p = 0.03, paired test; τs = 282 ± 33 ms in Cntr vs 209 ± 18 ms in Ro, p = 0.07, paired *t*-test; $A_f = 0.79 \pm 0.03$ ms in Cntr vs 0.80 ± 0.03 ms in Ro, p = 0.83, paired *t*-test. Despite the likely underestimation due to rundown (cf 12% inhibition with vehicle), the NMDAR EPSC amplitude and total charge in FHM2 mice in the presence of Ro are similar to those in WT mice (WT amplitude: 145 ± 14 pA, n = 22, p = 0.22, *t*-test; WT charge: 9.9 ± 1.3 pA, p = 0.28 *t*-test); also similar are the decay kinetics of the NMDAR EPSC in FHM2 with Ro and WT mice (WT $t_{1/2} = 38 \pm 2$ ms, p = 0.24 *t*-test).
C Percentage of inhibition of the FHM2 NMDAR EPSC after application for 20–25 min of Ro25 at two different concentrations (1 μM and 20 μM): 48 ± 6% Ro 1 μM and 71 ± 3% Ro 20 μM (p = 0.003, *t*-test; p = 0.002 paired *t*-test for Ro 1 μM relative to baseline and p = 0.0004 paired *t*-test for Ro 20 uM relative to baseline). Most likely, in both cases, the % inhibition by 20 μM Ro25 is somewhat overestimated due to rundown in the long recordings. The dotted lines in the bars indicate the % inhibition by vehicle after 20–25 min, which likely provides an approximation of the overestimation.

and statistics). Accordingly, the decay kinetics of the NMDAR EPSC were faster in the presence of Ro25 in FHM2 mice and were not significantly different from those in WT mice (Fig. 5B). The half-time of decay was 13 ± 4% smaller in Ro compared to control. The time constants of the fast and slow exponentials best fitting the decay were both smaller in Ro (by 16 ± 5% in the case of τf and 22 ± 9% in the case of τs), while their relative amplitudes were similar in Ro and control; the weighted time constant, τw, was 22 ± 2% smaller in Ro (Fig. 5B, see legend for average values and statistics).

We also measured the fraction of the NMDAR EPSC that was inhibited by 20 μM Ro25 in FHM2 mice, which, as expected, was larger than that in WT mice (71 ± 3%, p = 0.02 *t*-test; Fig. 5C). Most likely, the % inhibition by 20 μM Ro25 is somewhat overestimated in both WT and FHM2 slices due to rundown in long recordings lasting at least 30 min. Assuming that the overestimation due to rundown is similar to the 12% inhibition by vehicle and correcting for it, the average inhibition by 20 uM Ro in FHM2 mice (59%) is only slightly smaller than the 66% inhibition predicted if we sum the % inhibition by 1 uM Ro in FHM2 mice (36%, reflecting the contribution of diheteromeric GluN2B receptors) and the % inhibition derived from the % inhibition by Ro 20 uM in WT mice assuming that the same amount (pA) of NMDA EPSC is due to triheteromeric GluN2B-N2A receptors in the two genotypes (30%, from % inhib Ro 20 in WT × $EPSC_{WT}/EPSC_{FHM2}$ = 43 × 145/211). Likely, a different extent of rundown in different set of experiments and an imperfect correction of it using the vehicle data account for the small difference between the predicted and the experimental % inhibition by 20 uM Ro in FHM2.

Overall, our pharmacological data are consistent with the conclusion that, in agreement with the proposed role of extrasynaptic diheteromeric GluN1-N2B NMDARs as primary detectors of glutamate spillover (Scimemi et al., 2004; Scimemi et al., 2009), the reduced rate of glutamate clearance produced by the FHM2 mutation mainly leads to enhanced activation of extrasynaptic GluN1-N2B NMDARs. Consistent with and supporting this conclusion are also the unaltered levels of GluN2A and GluN2B subunits in the cortex of FHM2 mice revealed by Western blottings (Supplementary Fig. 2), which rule out an increased expression of GluN1-N2B NMDARs at FHM2 synapses as a possible alternative interpretation.

3.4. *Preferential inhibition of GluN1-N2B NMDARs rescues the facilitation of CSD induction and propagation in FHM2 mice*

We then asked the question: is the enhanced susceptibility to experimental CSD in FHM2 mice due to specific activation of GluN1-N2B NMDARs? To answer this question we investigated the effect of 1 μM Ro25 on CSD induced in FHM2 slices by brief pulses of high K^+ (as in (Capuani et al., 2016)). Pressure-ejection KCl pulses of increasing duration were applied (at 5-min intervals) onto the slice surface (layer 2/3) until a CSD was elicited, as revealed by the associated changes in intrinsic optic signal (IOS). The duration of the first pulse eliciting a CSD was taken as CSD threshold and the rate of horizontal spread of the change in IOS as CSD propagation velocity (Fig. 6A). The threshold for CSD induction was 41% higher and the velocity of CSD propagation was 18% lower in the presence of Ro25 (1 μM, applied for 25 min before the KCl pulses) compared to the CSD threshold and velocity in control slices perfused with vehicle (Fig. 6B).

The values of CSD threshold and velocity in FHM2 slices in the presence of Ro25 were similar to those in control WT slices perfused with vehicle (Fig. 6B). In WT mice, Ro25 (1 μM) did not significantly affect the CSD threshold (234 ± 11 ms, n = 16, N = 8 p = 0.27 MW test), but it decreased by 13% the CSD velocity (2.82 ± 0.09 mm/min, n = 16, N = 8, p = 0.006, *t*-test) (data not shown). Our finding that preferential inhibition of diheteromeric GluN1-N2B NMDARs rescues most of the facilitation of CSD induction and propagation in FHM2 mice supports the conclusion that the enhanced susceptibility to experimental CSD in FHM2 mice is due to specific activation of GluN1-N2B NMDARs.

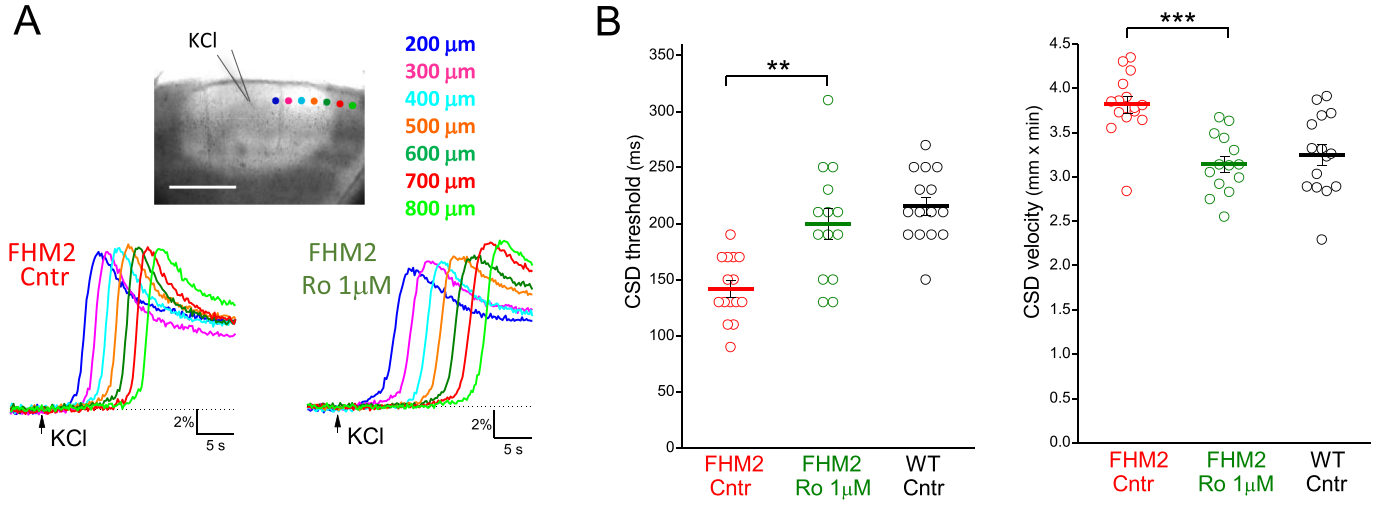

Fig. 6. Preferential inhibition of diheteromeric GluN1-N2B NMDARs rescues the facilitation of CSD induction and propagation in FHM2 mice.
A Image of a cortical slice after pressure ejection of a high KCl pulse which elicits a CSD, showing the typical change in light transmittance associated with a spreading CSD (top panel; scale bar: 500 μm), and representative changes in intrinsic optical signal (IOS) relative to background measured during CSD propagation at increasing times and distances (ROI: 30 μm diameter) from the KCl puff (as indicated in color code in the image on the top) in FHM2 slices after 20 min perfusion with vehicle (Cntr) and Ro25 (Ro 1 μM). The velocity of CSD propagation, obtained from the rate of horizontal spread of the change in IOS, in these two representative Cntr and Ro FHM2 slices is 4.3 and 3.1 mm/min, respectively.
B Stimulation threshold for CSD induction (CSD threshold) and rate of CSD propagation (CSD velocity) in Cntr FHM2 slices (n = 15; N = 8), FHM2 slices in the presence of Ro25 (n = 14; N = 8) and Cntr WT slices (n = 15; N = 8). CSD threshold is expressed as duration of the first KCl pulse eliciting a CSD. CSD threshold is higher and CSD velocity is lower in FHM2 slices in the presence of Ro compared to Cntr FHM2 slices. Average values of CSD threshold 200 ± 14 ms in Ro vs 142 ± 7 ms in vehicle, (p = 0.0015, MW test); CSD velocity: 3.15 ± 0.09 mm/min in Ro vs 3.82 ± 0.09 mm/min in vehicle, (p < 0.0001, *t*-test). CSD threshold and velocity in FHM2 slices in the presence of Ro are similar to those in Cntr WT slices (WT threshold: 215 ± 8 ms, p = 0.30, MW test; WT velocity: 3.25 ± 0.12 mm/min, p = 0.49 *t*-test).

4. Discussion

The main new findings of this study can be summarized as follows. The relatively small slowing of glutamate clearance, due to impairment of glutamate uptake into astrocytes, in FHM2 compared to WT mice (Capuani et al., 2016) results in increased amplitude and slowing of both rise time and decay of the NMDAR EPSC elicited in L2/3 pyramidal cells of barrel cortex by (even low frequency) stimulation of neuronal afferents in L1. As a consequence, the total charge carried by NMDARs is much increased in FHM2 compared to WT mice. A low concentration of the allosteric antagonist of GluN2B-containing NMDARs Ro25 (1 μM), which should inhibit diheteromeric GluN1-N2B and only a minor fraction of triheteromeric GluN1-N2A-N2B NMDARs (Volianskis et al., 2013; Stroebel et al., 2018), hardly affects the NMDAR EPSC in WT mice, but rescues the increased and prolonged activation of NMDARs as well as the facilitation of CSD induction and propagation in FHM2 mice.

Considering the large fraction of the NMDAR EPSC which is inhibited by a higher concentration of Ro25 (20 uM) in our juvenile WT mice, the synaptic NMDARs that are activated in L2/3 pyramidal cells by L1 stimulation appear to be mainly constituted by triheteromeric GluN1-N2A-N2B NMDARs (cf also decay kinetics of the NMDAR EPSC, which are similar to those of recombinant and hippocampal GluN1-N2A-N2B receptors (Hansen et al., 2014) (Tovar et al., 2013)). Thus, the finding that the increase in amplitude and slowing of the kinetics of the NMDAR EPSC in FHM2 mice is largely inhibited by 1 uM Ro25 suggests that the increased glutamate spillover and increased dwell time of glutamate in the extracellular space consequent to the reduced uptake of glutamate by astrocytes in FHM2 mice mainly lead to activation of extrasynaptic NMDARs consisting of diheteromeric GluN1-N2B receptors. This is consistent with the higher affinity for glutamate (and lower susceptibility to Mg block) of GluN1-N2B compared to GluN1-N2A-N2B receptors (Stroebel et al., 2014; Stroebel et al., 2018) and with the proposed role for extrasynaptic GluN1-N2B NMDARs as primary detectors of glutamate spillover (Scimemi et al., 2004; Scimemi et al., 2009). Also triheteromeric GluN1-N2B-N2D receptors are partially inhibited by 1 μM Ro25 and have even higher affinity for glutamate (and lower susceptibility to Mg block) than GluN1-N2B receptors (Yi et al., 2019). However, the GluN2D subunit is expressed mainly in inhibitory interneurons and appears to be absent or expressed very little in pyramidal cells (Standaert et al., 1996; Engelhardt et al., 2015; Garst-Orozco et al., 2020).

In agreement with the activity-dependence of the slowing of glutamate clearance in FHM2 mice, revealed by STC measured in L1 astrocytes of barrel cortex (Capuani et al., 2016) and here confirmed by measurements of L1 extracellular glutamate transients, the increased activation of NMDARs in FHM2 mice is activity-dependent. Both the increase in amplitude and the slowing of the decay of the NMDAR EPSC in FHM2 compared to WT mice were larger with high frequency compared to low frequency afferent activity (resulting in a 65% relatively larger gain-of-function of the total charge carried by NMDARs with high frequency compared to low frequency activity in FHM2 mice).

High-frequency repetitive and/or synchronous activity of nearby synapses promote the generation of dendritic NMDA spikes (local long-lasting regenerative depolarizations in apical tuft and basal dendrites caused by activation of enough NMDA receptors in a small area) (Schiller et al., 2000) (Nevian et al., 2007; Larkum et al., 2009; Major et al., 2013). The NMDARs involved in generation of NMDA spikes include extrasynaptic NMDARs activated by glutamate spillover, and pharmacological reduction of glutamate clearance lowers the stimulation threshold that elicits dendritic spikes in WT mice (Chalifoux and Carter, 2011; Brandalise et al., 2016). Thus, on the basis of our present data, we can predict that the FHM2 mutation may lower the threshold for ignition of NMDA spikes in the apical dendrites of L2/3 pyramidal cells in the barrel cortex. We have recently shown that this indeed occurs in the cingulate cortex, where the generation of NMDA spikes in the tuft dendrites of L5 pyramidal cells is facilitated in FHM2 mice and, as a consequence, the output firing of these neurons is enhanced, a finding with important implications in the context of migraine pain (Romanos et al., 2020). In fact, astrocyte-specific compensation of the defective α_2NKA in the cingulate cortex in FHM2 mice, which prevented the facilitation of NMDA spikes and output firing in pyramidal neurons, reduced the sensitivity of the mutant mice to a migraine-relevant head pain trigger (Romanos et al., 2020). The likely facilitation of dendritic NMDA spikes in sensory cortices in FHM2 would also have interesting implications in the context of migraine. In fact, dendritic NMDA spikes evoked in vivo during sensory input were shown to strongly influence context-dependent sensory gain and perception (Smith et al., 2013; Manita et al., 2015; Takahashi et al., 2016; Manita et al., 2017; Takahashi et al., 2020), suggesting that a dysfunctional regulation of NMDA spikes generation in apical dendrites of pyramidal cells in sensory cortices might contribute to the altered processing of sensory information revealed in migraineurs during the interictal period (Brennan and Pietrobon, 2018). Dendritic NMDA spikes are also involved in associative LTP and experience-dependent synaptic plasticity in vivo (Gambino et al., 2014; Cichon and Gan, 2015; Brandalise et al., 2016), and long-term-potentiation induced by high frequency stimulation at the hippocampal perforant path synapses in the dentate gyrus is enhanced in FHM2 mice (Iure et al., 2019).

As mentioned in the introduction, the impaired rate of glutamate clearance in the FHM2 mouse model as well as the enhanced $Ca_V2.1$-dependent glutamate release in the FHM1 mouse model can largely account for the decreased CSD threshold in the FHM mice (Tottene et al., 2009; Capuani et al., 2016). These findings, together with the strong pharmacological support for a key role of NMDARs in initiation of experimental CSD at the induction site (Pietrobon and Moskowitz, 2014; Sanchez-Porras et al., 2014; Shatillo et al., 2015; Chung et al., 2018), led us to propose a model of CSD ignition in which the depolarizing stimulus releases enough glutamate to overwhelm the binding capacity of astrocytic glutamate transporters, thus leading to cooperative activation of synaptic and extrasynaptic NMDARs in a number sufficient to initiate the positive feedback cycle that ignites a CSD. According to this model, increased susceptibility to CSD in both FHM1 and FHM2 is due to the fact that the glutamate threshold and the threshold activation of NMDARs necessary for CSD ignition are reached with stimuli of lower intensity (Tottene et al., 2009; Pietrobon and Moskowitz, 2014; Capuani et al., 2016; Pietrobon and Brennan, 2019).This model is supported by our present findings showing activity-dependent enhanced activation of NMDARs in FHM2 mice, whose inhibition rescues the facilitation of CSD initiation, as well as the recent evidence that CSD ignites at similar threshold levels of glutamate and glutamatergic plumes in awake WT and FHM2 mice, but these threshold levels are reached at a lower stimulation intensity in FHM2 mice (Parker et al., 2021). Our present data suggest that the enhanced susceptibility to CSD in FHM2 is mainly due to specific activation of extrasynaptic GluN1-N2B receptors. In fact, activation of these receptors is specifically enhanced in FHM2 mice by relatively low intensity stimulation and preferential inhibition of GluN1-N2B receptors rescues most of the facilitation of CSD induction and propagation in FHM2 mice.

Preferential inhibition of GluN1-N2B receptors did not significantly increase the CSD threshold in WT mice, but it decreased by 13% the rate of CSD propagation. According to preliminary findings showing a large increase in CSD threshold and decrease in CSD velocity in the presence of 20 μM Ro25 (data not shown), CSD initiation and propagation in WT mice appear to depend mainly on activation of synaptic triheteromeric GluN1-N2A-N2B receptors. Previous in vivo pharmacology using systemic injection of antagonists of GluN2B-containing NMDARs provided evidence for the contribution of these receptors to CSD initiation and propagation in WT animals; it remains unclear whether triheteromeric GluN1-N2A-N2B receptors were partially inhibited by the concentration of antagonist reached in the brain in these studies (Menniti et al., 2000; Peeters et al., 2007; Shatillo et al., 2015).

In migraineurs CSD is not induced by experimental depolarizing

stimuli, but arises "spontaneously" in certain conditions. Our findings suggest that ignition of a "spontaneous" CSD could be favoured by conditions leading to excessive activation of extrasynaptic NMDARs, i.e. conditions leading to glutamate spillover and membrane depolarization; these conditions would elevate local extracellular glutamate and/or glutamatergic plumes above the threshold level (Parker et al., 2021) necessary to activate a sufficient number of NMDARs and ignite CSD. This would probably require high-frequency repetitive or synchronous activity of a sufficient number of excitatory synapses in which glutamatergic transmission is potentiated, e.g. due to increased glutamate release (as in FHM1) or reduced expression of astrocytic α_2NKA and glutamate transporters (as in FHM2) or other mechanisms in common migraine. We hypothesize that this may occur in certain conditions as a consequence of dysfunctional regulation of the E/I balance in specific cortical circuits (Vecchia and Pietrobon, 2012).

If our suggestions regarding the conditions favouring ignition of a "spontaneous" CSD are correct and if, in human visual cortex, where most of the spontaneous CSDs arise (Pietrobon and Moskowitz, 2014), the relevant extrasynaptic NMDARs in apical dendrites are GluN1-N2B receptors, then specific inhibition of these receptors might be effective in preventing CSD in migraineurs with limited or no adverse effects. In fact, selective antagonists of GluN2B-containing NMDARs, at sufficiently low doses, did not show in humans the adverse acute psychotomimetic effects of low doses of ketamine, a high-affinity open channel blocker of NMDARs (Krystal et al., 1994; MERCHANT et al., 1999; Preskorn et al., 2008; Ibrahim et al., 2012). Interestingly, 1 μM Ro 25 did not produce, unlike ketamine, acute disinhibition of pyramidal cells and consequent increase in their synaptically driven firing in mouse hippocampal slices (Widman and McMahon, 2018). The recent reports that decreased glutamate transporter GLT-1 expression and increased GluN2B tyrosine phosphorylation have a key role in central sensitization and mechanical allodynia in a rat model of chronic migraine (Wang et al., 2018; Zhou et al., 2020) suggest that specific inhibition of GluN2B-containing NMDARs might also be effective in preventing prolonged migraine pain (and perhaps migraine chronicity) (Pietrobon and Moskowitz, 2013; Burstein et al., 2015; Brennan and Pietrobon, 2018).

While to our knowledge there are no clinical studies testing the effect of selective GluN2B antagonists on migraineurs, some recent small double-blind placebo-controlled paralle-group studies have shown efficacy of memantine, a low affinity open channel blocker of NMDARs, in reducing the attack frequency and number of days with headache as well as headache severity in migraine without aura patients (as well as the frequency of aura in a retrospective case series study including migraine with aura patients) (Charles et al., 2007; Noruzzadeh et al., 2016; Shanmugam et al., 2019), with very mild transient adverse effects in only a minority of patients. Interestingly, in contrast with high-affinity open channel blockers, memantine at low therapeutic doses has been reported to preferentially block extrasynaptic NMDARs while relatively sparing synaptic NMDARs (Xia et al., 2010; Gideons et al., 2014; Johnson et al., 2015).

Author statement

GC, AT, MV, MM, and MS performed the experiments, analyzed the data, discussed interpretation of the data, and revised critically the manuscript. MS contributed to the experimental design, discussed interpretation of the data, and revised critically the manuscript. GCb provided the FHM2 mouse model and revised critically the manuscript. FC supervised the experiments, discussed interpretation of the data and revised critically the manuscript. DP designed the study, supervised the experiments, interpreted the data and wrote the manuscript. All authors have read and approved the manuscript.

Acknowledgments

This work was supported by Telethon Italy Grant GGP14234 and Italian Ministry of University and Research PRIN 2017ANP5L8 to D.P., and by UNIVPM grant PSA 2017 to F.C.

Declaration of interest

None.

Appendix A. Supplementary data

Supplementary data to this article can be found online at https://doi.org/10.1016/j.nbd.2021.105419.

References

Armbruster, M., Hanson, E., Dulla, C.G., 2016. Glutamate clearance is locally modulated by presynaptic neuronal activity in the cerebral cortex. J. Neurosci. 36, 10404–10415.
Arnth-Jensen, N., Jabaudon, D., Scanziani, M., 2002. Cooperation between independent hippocampal synapses is controlled by glutamate uptake. Nat. Neurosci. 5, 325–331.
Bradford, M.M., 1976. A rapid and sensitive method for the quantitation of microgram quantities of protein utilizing the principle of protein-dye binding. Anal. Biochem. 72, 248–254.
Bragina, L., Melone, M., Fattorini, G., Torres-Ramos, M., Vallejo-Illarramendi, A., Matute, C., Conti, F., 2006. GLT-1 down-regulation induced by clozapine in rat frontal cortex is associated with synaptophysin up-regulation. J. Neurochem. 99, 134–141.
Brandalise, F., Carta, S., Helmchen, F., Lisman, J., Gerber, U., 2016. Dendritic NMDA spikes are necessary for timing-dependent associative LTP in CA3 pyramidal cells. Nat. Commun. 7, 13480.
Brennan, K.C., Pietrobon, D., 2018. A systems neuroscience approach to migraine. Neuron 97, 1004–1021.
Burstein, R., Noseda, R., Borsook, D., 2015. Migraine: multiple processes, complex pathophysiology. J. Neurosci. 35, 6619–6629.
Capuani, C., Melone, M., Tottene, A., Bragina, L., Crivellaro, G., Santello, M., Casari, G., Conti, F., Pietrobon, D., 2016. Defective glutamate and K⁺ clearance by cortical astrocytes in familial hemiplegic migraine type 2. EMBO Mol. Med. 8, 967–986.
Chalifoux, J.R., Carter, A.G., 2011. Glutamate spillover promotes the generation of NMDA spikes. J. Neurosci. 31, 16435–16446.
Charles, A., Flippen, C., Romero Reyes, M., Brennan, K.C., 2007. Memantine for prevention of migraine: a retrospective study of 60 cases. J. Headache Pain 8, 248–250.
Chung, D.Y., Sugimoto, K., Fischer, P., Bohm, M., Takizawa, T., Sadeghian, H., Morais, A., Harriott, A., Oka, F., Qin, T., Henninger, N., Yaseen, M.A., Sakadzic, S., Ayata, C., 2018. Real-time non-invasive in vivo visible light detection of cortical spreading depolarizations in mice. J. Neurosci. Methods 309, 143–146.
Cichon, J., Gan, W.-B., 2015. Branch-specific dendritic Ca2+ spikes cause persistent synaptic plasticity. Nature 520, 180–185.
Danbolt, N.C., Pines, G., Kanner, B.I., 1990. Purification and reconstitution of the sodium- and potassium-coupled glutamate transport glycoprotein from rat brain. Biochemistry 29, 6734–6740.
De Fusco, M., Marconi, R., Silvestri, L., Atorino, L., Rampoldi, L., Morgante, L., Ballabio, A., Aridon, P., Casari, G., 2003. Haploinsufficiency of ATP1A2 encoding the Na+/K+ pump alpha2 subunit associated with familial hemiplegic migraine type 2. Nat. Genet. 33, 192–196.
Diamond, J.S., 2005. Deriving the glutamate clearance time course from transporter currents in CA1 hippocampal astrocytes: transmitter uptake gets faster during development. J. Neurosci. 25, 2906–2916.
Dichgans, M., Freilinger, T., Eckstein, G., Babini, E., Lorenz-Depiereux, B., Biskup, S., Ferrari, M.D., Herzog, J., van den Maagdenberg, A.M., Pusch, M., Strom, T.M., 2005. Mutation in the neuronal voltage-gated sodium channel SCN1A in familial hemiplegic migraine. Lancet 366, 371–377.
Dugue, G.P., Dumoulin, A., Triller, A., Dieudonne, S., 2005. Target-dependent use of co-released inhibitory transmitters at central synapses. J. Neurosci. 25, 6490–6498.
Eikermann-Haerter, K., Dilekoz, E., Kudo, C., Savitz, S.I., Waeber, C., Baum, M.J., Ferrari, M.D., van den Maagdenberg, A.M.J.M., Moskowitz, M.A., Ayata, C., 2009. Genetic and hormonal factors modulate spreading depression and transient hemiparesis in mouse models of familial hemiplegic migraine type 1. J. Clin. Investig. 119, 99–109.
Engelhardt, J.V., Bocklisch, C., Tönges, L., Herb, A., Mishina, M., Monyer, H., 2015. GluN2D-containing NMDA receptors-mediate synaptic currents in hippocampal interneurons and pyramidal cells in juvenile mice. Front. Cell. Neurosci. 9.
Filiz, A., Tepe, N., Eftekhari, S., Boran, H.E., Dilekoz, E., Edvinsson, L., Bolay, H., 2019. CGRP receptor antagonist MK-8825 attenuates cortical spreading depression induced pain behavior. Cephalalgia 39, 354–365.
Gambino, F., Pagès, S., Kehayas, V., Baptista, D., Tatti, R., Carleton, A., Holtmaat, A., 2014. Sensory-evoked LTP driven by dendritic plateau potentials in vivo. Nature 515, 116–119.
Garst-Orozco, J., Malik, R., Lanz, T.A., Weber, M.L., Xi, H., Arion, D., Enwright 3rd, J.F., Lewis, D.A., O'Donnell, P., Sohal, V.S., Buhl, D.L., 2020. GluN2D-mediated excitatory drive onto medial prefrontal cortical PV+ fast-spiking inhibitory interneurons. PLoS One 15, e0233895.

Gideons, E.S., Kavalali, E.T., Monteggia, L.M., 2014. Mechanisms underlying differential effectiveness of memantine and ketamine in rapid antidepressant responses. Proc. Natl. Acad. Sci. 111, 8649–8654.
Goadsby, P.J., Holland, P.R., Martins-Oliveira, M., Hoffmann, J., Schankin, C., Akerman, S., 2017. Pathophysiology of migraine: a disorder of sensory processing. Physiol. Rev. 97, 553–622.
Gray, J.A., Shi, Y., Usui, H., During, M.J., Sakimura, K., Nicoll, R.A., 2011. Distinct modes of AMPA receptor suppression at developing synapses by GluN2A and GluN2B: single-cell NMDA receptor subunit deletion in vivo. Neuron 71, 1085–1101.
Hansen, K.B., Ogden, K.K., Yuan, H., Traynelis, S.F., 2014. Distinct functional and pharmacological properties of Triheteromeric GluN1/GluN2A/GluN2B NMDA receptors. Neuron 81, 1084–1096.
Hanson, E., Armbruster, M., Cantu, D., Andresen, L., Taylor, A., Danbolt, N.C., Dulla, C. G., 2015. Astrocytic glutamate uptake is slow and does not limit neuronal NMDA receptor activation in the neonatal neocortex. Glia 63, 1784–1796.
Harney, S.C., Jane, D.E., Anwyl, R., 2008. Extrasynaptic NR2D-containing NMDARs are recruited to the synapse during LTP of NMDAR-EPSCs. J. Neurosci. 28, 11685–11694.
Harriott, A.M., Chung, D.Y., Uner, A., Bozdayi, R.O., Morais, A., Takizawa, T., Qin, T., Ayata, C., 2021. Optogenetic spreading depression elicits trigeminal pain and anxiety behavior. Ann. Neurol. 89, 99–110.
Ibrahim, L., DiazGranados, N., Jolkovsky, L., Brutsche, N., Luckenbaugh, D.A., Herring, W.J., Potter, W.Z., Zarate, C.A.J., 2012. A randomized, placebo-controlled, crossover pilot trial of the Oral selective NR2B antagonist MK-0657 in patients with treatment-resistant Major depressive disorder. J. Clin. Psychopharmacol. 32, 551–557.
Iure, A., Mazzocchetti, P., Bastioli, G., Picconi, B., Costa, C., Marchionni, I., Casari, G., Tozzi, A., Pietrobon, D., Calabresi, P., 2019. Differential effect of FHM2 mutation on synaptic plasticity in distinct hippocampal regions. Cephalalgia 333102419839967.
Jansen, N.A., Dehghani, A., Linssen, M.M.L., Breukel, C., Tolner, E.A., van den Maagdenberg, A.M.J.M., 2020. First FHM3 mouse model shows spontaneous cortical spreading depolarizations. Ann. Clin. Transl. Neurol. 7, 132–138.
Johnson, J.W., Glasgow, N.G., Povysheva, N.V., 2015. Recent insights into the mode of action of memantine and ketamine. Curr. Opin. Pharmacol. 20, 54–63.
Kros, L., Lykke-Hartmann, K., Khodakhah, K., 2018. Increased susceptibility to cortical spreading depression and epileptiform activity in a mouse model for FHM2. Sci. Rep. 8, 16959.
Krystal, J.H., Karper, L.P., Seibyl, J.P., Freeman, G.K., Delaney, R., Bremner, J.D., Heninger, G.R., Bowers Jr., M.B., Charney, D.S., 1994. Subanesthetic effects of the noncompetitive NMDA antagonist, ketamine, in humans: psychotomimetic, perceptual, cognitive, and neuroendocrine responses. Arch. Gen. Psychiatry 51, 199–214.
Kutsuwada, T., Kashiwabuchi, N., Mori, H., Sakimura, K., Kushiya, E., Araki, K., Meguro, H., Masaki, H., Kumanishi, T., Arakawa, M., et al., 1992. Molecular diversity of the NMDA receptor channel. Nature 358, 36–41.
Larkum, M.E., Nevian, T., Sandler, M., Polsky, A., Schiller, J., 2009. Synaptic integration in tuft dendrites of layer 5 pyramidal neurons: a new unifying principle. Science 325, 756–760.
Leo, L., Gherardini, L., Barone, V., De Fusco, M., Pietrobon, D., Pizzorusso, T., Casari, G., 2011. Increased susceptibility to cortical spreading depression in the mouse model of familial hemiplegic migraine type 2. PLoS Genet. 7, e1002129.
Li, R., Shen, Y., 2013. An old method facing a new challenge: re-visiting housekeeping proteins as internal reference control for neuroscience research. Life Sci. 92, 747–751.
Major, G., Larkum, M.E., Schiller, J., 2013. Active properties of neocortical pyramidal neuron dendrites. Annu. Rev. Neurosci. 36, 1–24.
Manita, S., Suzuki, T., Homma, C., Matsumoto, T., Odagawa, M., Yamada, K., Ota, K., Matsubara, C., Inutsuka, A., Sato, M., Ohkura, M., Yamanaka, A., Yanagawa, Y., Nakai, J., Hayashi, Y., Larkum, M.E., Murayama, M., 2015. A top-down cortical circuit for accurate sensory perception. Neuron 86, 1304–1316.
Manita, S., Miyakawa, H., Kitamura, K., Murayama, M., 2017. Dendritic spikes in sensory perception. Front. Cell. Neurosci. 11.
Marvin, J.S., Borghuis, B.G., Tian, L., Cichon, J., Harnett, M.T., Akerboom, J., Gordus, A., Renninger, S.L., Chen, T.-W., Bargmann, C.I., Orger, M.B., Schreiter, E.R., Demb, J. B., Gan, W.-B., Hires, S.A., Looger, L.L., 2013. An optimized fluorescent probe for visualizing glutamate neurotransmission. Nat. Methods 10, 162–170.
Meguro, H., Mori, H., Araki, K., Kushiya, E., Kutsuwada, T., Yamazaki, M., Kumanishi, T., Arakawa, M., Sakimura, K., Mishina, M., 1992. Functional characterization of a heteromeric NMDA receptor channel expressed from cloned cDNAs. Nature 357, 70–74.
Melone, M., Vitellaro-Zuccarello, L., Vallejo-Illarramendi, A., Perez-Samartin, A., Matute, C., Cozzi, A., Pellegrini-Giampietro, D.E., Rothstein, J.D., Conti, F., 2001. The expression of glutamate transporter GLT-1 in the rat cerebral cortex is down-regulated by the antipsychotic drug clozapine. Mol. Psychiatry 6, 380–386.
Menniti, F.S., Pagnozzi, M.J., Butler, P., Chenard, B.L., Jaw-Tsai, S.S., Frost White, W., 2000. CP-101,606, an NR2B subunit selective NMDA receptor antagonist, inhibits NMDA and injury induced c-fos expression and cortical spreading depression in rodents. Neuropharmacology 39, 1147–1155.
Merchant, R.E., Bullock, M.R., Carmack, C.A., Shah, A.K., Wilner, K.D., Ko, G., Williams, S.A., 1999. A double-blind, placebo-controlled study of the safety, tolerability and pharmacokinetics of CP-101,606 in patients with a mild or moderate traumatic brain injury. Ann. N. Y. Acad. Sci. 890, 42–50.
Neher, E., 1992. Correction for liquid junction potentials in patch clamp experiments. Methods Enzymol. 207, 123–131.
Nevian, T., Larkum, M.E., Polsky, A., Schiller, J., 2007. Properties of basal dendrites of layer 5 pyramidal neurons: a direct patch-clamp recording study. Nat. Neurosci. 10, 206–214.
Noruzzadeh, R., Modabbernia, A., Aghamollaii, V., Ghaffarpour, M., Harirchian, M.H., Salahi, S., Nikbakht, N., Noruzi, N., Tafakhori, A., 2016. Memantine for prophylactic treatment of migraine without Aura: a randomized double-blind placebo-controlled study. Headache 56, 95–103.
Ophoff, R.A., Terwindt, G.M., Vergouwe, M.N., van Eijk, R., Oefner, P.J., Hoffman, S.M. G., Lamerdin, J.E., Mohrenweiser, H.W., Bulman, D.E., Ferrari, M., Haan, J., Lindhout, D., van Hommen, G.-J.B., Hofker, M.H., Ferrari, M.D., Frants, R.R., 1996. Familial hemiplegic migraine and episodic ataxia type-2 are caused by mutations in the Ca^{2+} channel gene CACNL1A4. Cell 87, 543–552.
Paoletti, P., Bellone, C., Zhou, Q., 2013. NMDA receptor subunit diversity: impact on receptor properties, synaptic plasticity and disease. Nat. Rev. Neurosci. 14, 383–400.
Parker, P.D., Suryavanshi, P., Melone, M., Sawant-Pokam, P.A., Reinhart, K.M., Kaufmann, D., Theriot, J.J., Pugliese, A., Conti, F., Shuttleworth, C.W., Pietrobon, D., Brennan, K.C., 2021. Non-canonical glutamate signaling in a genetic model of migraine with aura. Neuron 109, 611–628 e618.
Peeters, M., Gunthorpe, M.J., Strijbos, L.M., Goldsmith, P., Upton, N., James, M.F., 2007. Effects of pan-and subtype-selective N-methyl-D-aspartate receptor antagonists on cortical spreading depression in the rat: therapeutic potential for migraine. J. Pharmacol. Exp. Ther. 321, 564–572.
Pietrobon, D., 2007. Familial hemiplegic migraine. Neurotherapeutics 4, 274–284.
Pietrobon, D., Brennan, K.C., 2019. Genetic mouse models of migraine. J. Headache Pain 20, 79.
Pietrobon, D., Moskowitz, M.A., 2013. Pathophysiology of migraine. Annu. Rev. Physiol. 75, 365–391.
Pietrobon, D., Moskowitz, M.A., 2014. Chaos and commotion in the wake of cortical spreading depression and spreading depolarizations. Nat. Rev. Neurosci. 15, 379–393.
Preskorn, S.H., Baker, B., Kolluri, S., Menniti, F.S., Krams, M., Landen, J.W., 2008. An innovative design to establish proof of concept of the antidepressant effects of the NR2B subunit selective N-methyl-D-aspartate antagonist, CP-101,606, in patients with treatment-refractory Major depressive disorder. J. Clin. Psychopharmacol. 28, 631–637.
Romanos, J., Benke, D., Saab, A.S., Zeilhofer, H.U., Santello, M., 2019. Differences in glutamate uptake between cortical regions impact neuronal NMDA receptor activation. Commun. Biol. 2, 127.
Romanos, J., Benke, D., Pietrobon, D., Zeilhofer, H.U., Santello, M., 2020. Astrocyte dysfunction increases cortical dendritic excitability and promotes cranial pain in familial migraine. Sci. Adv. 6, eaaz1584.
Sanchez-Porras, R., Santos, E., Scholl, M., Stock, C., Zheng, Z., Schiebel, P., Orakcioglu, B., Unterberg, A.W., Sakowitz, O.W., 2014. The effect of ketamine on optical and electrical characteristics of spreading depolarizations in gyrencephalic swine cortex. Neuropharmacology 84, 52–61.
Santello, M., Nevian, T., 2015. Dysfunction of cortical dendritic integration in neuropathic pain reversed by serotoninergic neuromodulation. Neuron 86, 233–246.
Schiller, J., Major, G., Koester, H.J., Schiller, Y., 2000. NMDA spikes in basal dendrites of cortical pyramidal neurons. Nature 404, 285–289.
Scimemi, A., Fine, A., Kullmann, D.M., Rusakov, D.A., 2004. NR2B-containing receptors mediate cross talk among hippocampal synapses. J. Neurosci. 24, 4767–4777.
Scimemi, A., Tian, H., Diamond, J.S., 2009. Neuronal transporters regulate glutamate clearance, NMDA receptor activation, and synaptic plasticity in the hippocampus. J. Neurosci. 29, 14581–14595.
Shanmugam, S., Karunaikadal, K., Varadarajan, S., Krishnan, M., 2019. Memantine ameliorates migraine headache. Ann. Indian Acad. Neurol. 22, 286–290.
Shatillo, A., Salo, R.A., Giniatullin, R., Grohn, O.H., 2015. Involvement of NMDA receptor subtypes in cortical spreading depression in rats assessed by fMRI. Neuropharmacology 93, 164–170.
Smith, S.L., Smith, I.T., Branco, T., Häusser, M., 2013. Dendritic spikes enhance stimulus selectivity in cortical neurons in vivo. Nature 503, 115–120.
Standaert, D.G., Landwehrmeyer, G.B., Kerner, J.A., Penney Jr., J.B., Young, A.B., 1996. Expression of NMDAR2D glutamate receptor subunit mRNA in neurochemically identified interneurons in the rat neostriatum, neocortex and hippocampus. Brain Res. Mol. Brain Res. 42, 89–102.
Stroebel, D., Carvalho, S., Grand, T., Zhu, S., Paoletti, P., 2014. Controlling NMDA receptor subunit composition using ectopic retention signals. J. Neurosci. 34, 16630–16636.
Stroebel, D., Casado, M., Paoletti, P., 2018. Triheteromeric NMDA receptors: from structure to synaptic physiology. Curr. Opin. Physiol. 2, 1–12.
Takahashi, N., Oertner, T.G., Hegemann, P., Larkum, M.E., 2016. Active cortical dendrites modulate perception. Science 354, 1587–1590.
Takahashi, N., Ebner, C., Sigl-Glöckner, J., Moberg, S., Nierwetberg, S., Larkum, M.E., 2020. Active dendritic currents gate descending cortical outputs in perception. Nat. Neurosci. 23, 1277–1285.
Tottene, A., Conti, R., Fabbro, A., Vecchia, D., Shapovalova, M., Santello, M., van den Maagdenberg, A.M.J.M., Ferrari, M.D., Pietrobon, D., 2009. Enhanced excitatory transmission at cortical synapses as the basis for facilitated spreading depression in Ca(v)2.1 Knockin migraine mice. Neuron 61, 762–773.
Tovar, K.R., McGinley, M.J., Westbrook, G.L., 2013. Triheteromeric NMDA receptors at hippocampal synapses. J. Neurosci. 33, 9150–9160.
Trabelsi, Y., Amri, M., Becq, H., Molinari, F., Aniksztejn, L., 2017. The conversion of glutamate by glutamine synthase in neocortical astrocytes from juvenile rat is important to limit glutamate spillover and peri/extrasynaptic activation of NMDA receptors. Glia 65, 401–415.

Tsukada, S., Iino, M., Takayasu, Y., Shimamoto, K., Ozawa, S., 2005. Effects of a novel glutamate transporter blocker, (2S, 3S)-3-[3-[4-(trifluoromethyl)benzoylamino] benzyloxy]aspartate (TFB-TBOA), on activities of hippocampal neurons. Neuropharmacology 48, 479–491.

Tzingounis, A.V., Wadiche, J.I., 2007. Glutamate transporters: confining runaway excitation by shaping synaptic transmission. Nat. Rev. Neurosci. 8, 935–947.

van den Maagdenberg, A.M., Pietrobon, D., Pizzorusso, T., Kaja, S., Broos, L.A., Cesetti, T., van de Ven, R.C., Tottene, A., van der Kaa, J., Plomp, J.J., Frants, R.R., Ferrari, M.D., 2004. A Cacna1a knockin migraine mouse model with increased susceptibility to cortical spreading depression. Neuron 41, 701–710.

van den Maagdenberg, A.M., et al., 2010. High cortical spreading depression susceptibility andmigraine-associated symptoms in Ca(v)2.1 S218L mice. Ann. Neurol. 67, 85–98.

Vecchia, D., Pietrobon, D., 2012. Migraine: a disorder of brain excitatory–inhibitory balance? Trends Neurosci. 35, 507–520.

Vecchia, D., Tottene, A., van den Maagdenberg, A.M.J.M., Pietrobon, D., 2015. Abnormal cortical synaptic transmission in CaV2.1 knockin mice with the S218L missense mutation which causes a severe familial hemiplegic migraine syndrome in humans. Front. Cell. Neurosci. 9.

Volianskis, A., Bannister, N., Collett, V.J., Irvine, M.W., Monaghan, D.T., Fitzjohn, S.M., Jensen, M.S., Jane, D.E., Collingridge, G.L., 2013. Different NMDA receptor subtypes mediate induction of long-term potentiation and two forms of short-term potentiation at CA1 synapses in rat hippocampus in vitro. J. Physiol. 591, 955–972.

Wang, X.-Y., Zhou, H.-R., Wang, S., Liu, C.-Y., Qin, G.-C., Fu, Q.-Q., Zhou, J.-Y., Chen, L.-X., 2018. NR2B-Tyr phosphorylation regulates synaptic plasticity in central sensitization in a chronic migraine rat model. J. Headache Pain 19, 102.

Watanabe, M., Fukaya, M., Sakimura, K., Manabe, T., Mishina, M., Inoue, Y., 1998. Selective scarcity of NMDA receptor channel subunits in the stratum lucidum (mossy fibre-recipient layer) of the mouse hippocampal CA3 subfield. Eur. J. Neurosci. 10, 478–487.

Widman, A.J., McMahon, L.L., 2018. Disinhibition of CA1 pyramidal cells by low-dose ketamine and other antagonists with rapid antidepressant efficacy. Proc. Natl. Acad. Sci. 115, E3007-E3016.

Xia, P., Chen, H-sv, Zhang, D., Lipton, S.A., 2010. Memantine preferentially blocks extrasynaptic over synaptic NMDA receptor currents in hippocampal autapses. J. Neurosci. 30, 11246–11250.

Yi, F., Bhattacharya, S., Thompson, C.M., Traynelis, S.F., Hansen, K.B., 2019. Functional and pharmacological properties of triheteromeric GluN1/2B/2D NMDA receptors. J. Physiol. 597, 5495–5514.

Zhou, X., Liang, J., Wang, J., Fei, Z., Qin, G., Zhang, D., Zhou, J., Chen, L., 2020. Up-regulation of astrocyte excitatory amino acid transporter 2 alleviates central sensitization in a rat model of chronic migraine. J. Neurochem. 155, 370–389.